Zürcher Hochschule
für Angewandte Wissenschaften

Life Sciences und
Facility Management

IUNR Institut für Umwelt und
Natürliche Ressourcen

Characterization of spatio-temporal thermal heterogeneity and riparian shading in the Glatt River using high-resolution thermal infrared and multispectral remote sensing

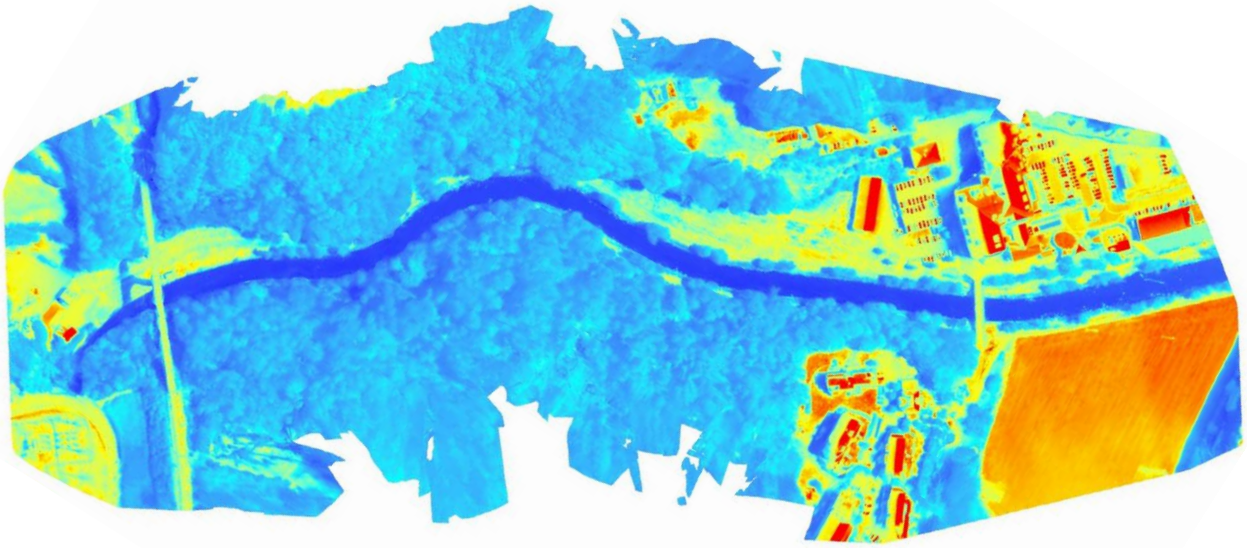

Institute of Natural Resource Sciences (IUNR),
Zurich University of Applied Sciences (ZHAW)

Commissioned by the Federal Office for the Environment (FOEN)

Wädenswil, January 2019

Imprint

Commissioned by
Federal Office for the Environment (FOEN), Hydrology Division, CH-3003 Bern. The FOEN is an agency of the Federal Department of the Environment, Transport, Energy and Communications (DETEC).

Contractor
Dr. Diego Tonolla, Zurich University of Applied Sciences (ZHAW), School of Life Sciences and Facility Management (LSFM), Institute of Natural Resource Sciences (IUNR).

Authors
Dr. Diego Tonolla, Dr. Johann Junghardt, Dr. Manuel Antonetti, Dr. Michael Döring.

FOEN support
Dr. Thilo Herold.

Suggested citation
Tonolla D, Junghardt J, Antonetti M, Döring M. 2019. Characterization of spatio-temporal thermal heterogeneity and riparian shading in the Glatt River using high-resolution thermal infrared and multispectral remote sensing.

Note
This study/report was prepared under contract to the Federal Office for the Environment (FOEN). The contractor bears sole responsibility for the content.

Figure title page
Thermal infrared (TIR) orthoimage of the Glatt River study reach acquired using a thermal camera mounted on a drone.

Table of Contents

1 Introduction

The FOEN continuously measures the water temperature of watercourses at around 80 measuring stations in Switzerland. Temperature is a major factor that influences physical, chemical, biological and ecological processes in aquatic ecosystems (Magnuson et al. 1979; Webb 1996; Caissie 2006), such as the dispersal of ectothermic organisms like fish, their behaviour and their survival (Buisson et al. 2008; McCullough et al. 2009). In hydromorphologically complex rivers, water temperature can vary greatly over time and space (Caissie 2006; Tonolla et al. 2010). Moreover, in the context of global warming, the importance of temperature is steadily increasing, since the thermal regime is changing and will continue to change at local, regional and global scales (IPCC 2014). The thermal regime of streams and rivers is primarily influenced by incoming shortwave solar radiation, air temperature, flow regime, riparian conditions, such as shade, streambed substrata and upwelling subsurface water, such as groundwater inflows (Webb & Zhang 1999; Malard et al. 2001; Webb et al. 2003). In addition, temperature loggers of automatic measuring stations are from time to time not sufficiently covered with water at periods of low discharge or can even fall completely dry. For these reasons, it is difficult to quantify spatio-temporal variability of water temperature exclusively using conventional *in-situ* methods (e.g. temperature loggers), in which case measurements with thermal infrared (TIR) sensors could be an effective alternative.

All bodies whose temperatures are above absolute zero (0 °K = -273.15 °C) emit thermal radiation. TIR sensors detect thermal radiation in the 3-5 and 7-14 µm wavelength range, which is emitted from the upper ~50 µm of any surface (Lillesand et al. 2008); thus allowing the radiation temperature to be determined. TIR imagery has already been successfully used to determine the spatial temperature heterogeneity of watercourses and floodplains (Faux et al. 2001; Torgersen et al. 2001; Cristea & Burges 2009; Tonolla et al. 2010, 2012; Wawrzyniak et al. 2013; Fricke & Baschek 2015; Fullerton et al. 2018), to identify areas of groundwater-surface water interactions (Loheide & Gorelick 2006; Deitchman & Loheide 2009; Eschbach et al. 2016; Wawrzyniak et al. 2016), to determine thermal mixing dynamics and velocity fields (Andrews et al. 2011; Cardenas et al. 2011), to calibrate and validate stream temperature models (Cristea & Burges 2009; Loheide & Gorelick 2006; Cardenas et al. 2014), to monitor the success of restoration projects (Shuman & Ambrose 2003; Loheide & Gorelick 2006) and

to identify warm and cold refuges critical for the survival of many biota, including fish (Madej et al. 2006; Torgersen et al. 1999, 2006; Tonolla et al. 2012; Fullerton et al. 2018).

The main advantage of TIR measurements over *in-situ* point measurements is their large-scale and non-invasive nature (i.e. you do not go into the water). When recording water temperature using TIR, however, various factors that may have a relevant influence on the measurements must be considered (Fig. 1). Particularly noteworthy examples of such factors are atmospheric absorption and emissions which are influenced by factors such as humidity, wind and sky radiation, the reflection of other objects near the watercourse (e.g. trees), emissivity (i.e. how much radiation is emitted by an object), surface characteristics (e.g. roughness, turbidity), mixed pixels (i.e. terrestrial-aquatic areas captured in a single thermal pixel) and the vertical stratification of the body of water (i.e. the different temperatures near the bottom and on the surface). For detailed summaries, see Dugdale et al. (2016) and the appendices in Tonolla et al. (2010, 2012).

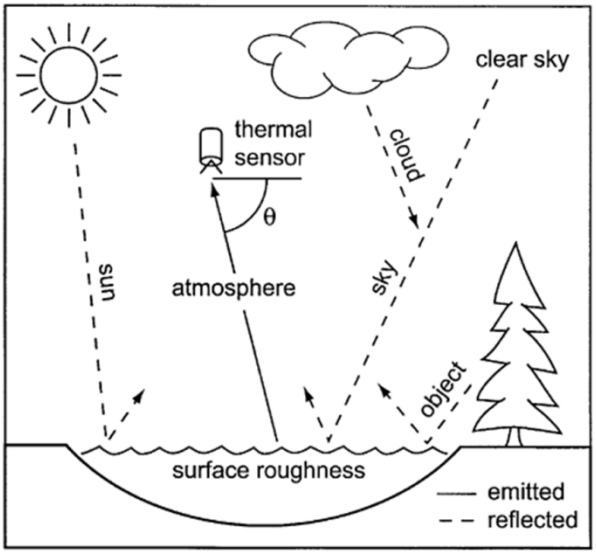

Figure 1. Sources of emitted and reflected TIR radiation in thermal remote sensing of rivers and streams. Image source: Torgersen et al. (2001).

One of the most important regulating factors in terms of water temperature is riparian vegetation (Rutherford et al. 1997; Caissie 2006). Vegetation cover can affect the heat flux by decreasing wind currents, altering the microclimate above the water surface (i.e. air temperature and relative humidity) and reducing penetration of solar radiation into the ground (increased absorption and reflection by the canopy). Since a reduction of shortwave solar radiation by either riparian vegetation or topography can significantly inhibit river warming (Rutherford et al. 1997, 2004; Johnson 2004), the spatio-temporal evolution of

riparian shading plays a key role in temperature regulation. High resolution remote sensing products are well suited to the spatial and temporal detection and quantification of shaded areas (Adeline et al. 2013). The emergence and sophistication of drone based remote sensing products represent a promising method for assessing the properties and effects of shading on small to medium river systems (Movia et al. 2016).

2 Objectives

The main aim of our study was to investigate the suitability of high-resolution thermal infrared and multispectral remote sensing for the characterization of spatio-temporal thermal heterogeneity and riparian vegetation shading. Our measurements were carried out in parallel and in coordination with other investigations (Bern University of Applied Sciences, Fischwerk environmental office) at a FOEN measuring station located on a hydromorphologically homogenous river. The results and empirical findings of these measurements are expected to contribute to the efficient mapping and monitoring of complex patterns of surface water temperature and riparian vegetation shading in river systems using the innovative tools presented in this manuscript.

3 Material and Methods

3.1 Study site and experimental design

The constrained, single thread reach of the 6th order Glatt River in canton Zurich (Switzerland; CH1903-LV03: 678040 / 269720) that was selected for this study is approximately 1.2 km long, has a mean average channel width of approximately 18 m and an average channel slope of approximately 7‰ (Fig. 2). A gauging station is located at the downstream end of the study reach (Glatt – Rheinsfelden; nr. 2415) at 336 m.a.s.l. and it has a catchment area of 417 km^2 with a mean elevation of 503 m.a.s.l. At this station, the mean annual water temperature in 2017 was 13.1 °C (range: 2.3 – 25.2 °C), the average discharge was 6.5 m^3/s (range: 2.7 – 38.2 m^3/s), HQ_2 was 55.8 m^3/s and HQ_{10} was 90.2 m^3/s, (FOEN 2018a). The Glatt joins the Rhine River approximately 260 m downstream from the gauging station. The flow regime of the Glatt at the station is “pluvial inférieur”. A wastewater treatment plant is located approximately 450 m upstream from the start of the reach. Nevertheless, the reach water is

rich in total phosphorous (100-130 µg P/L; FOEN 2018b) and a large number of macrophytes and algae grow on the river substrate.

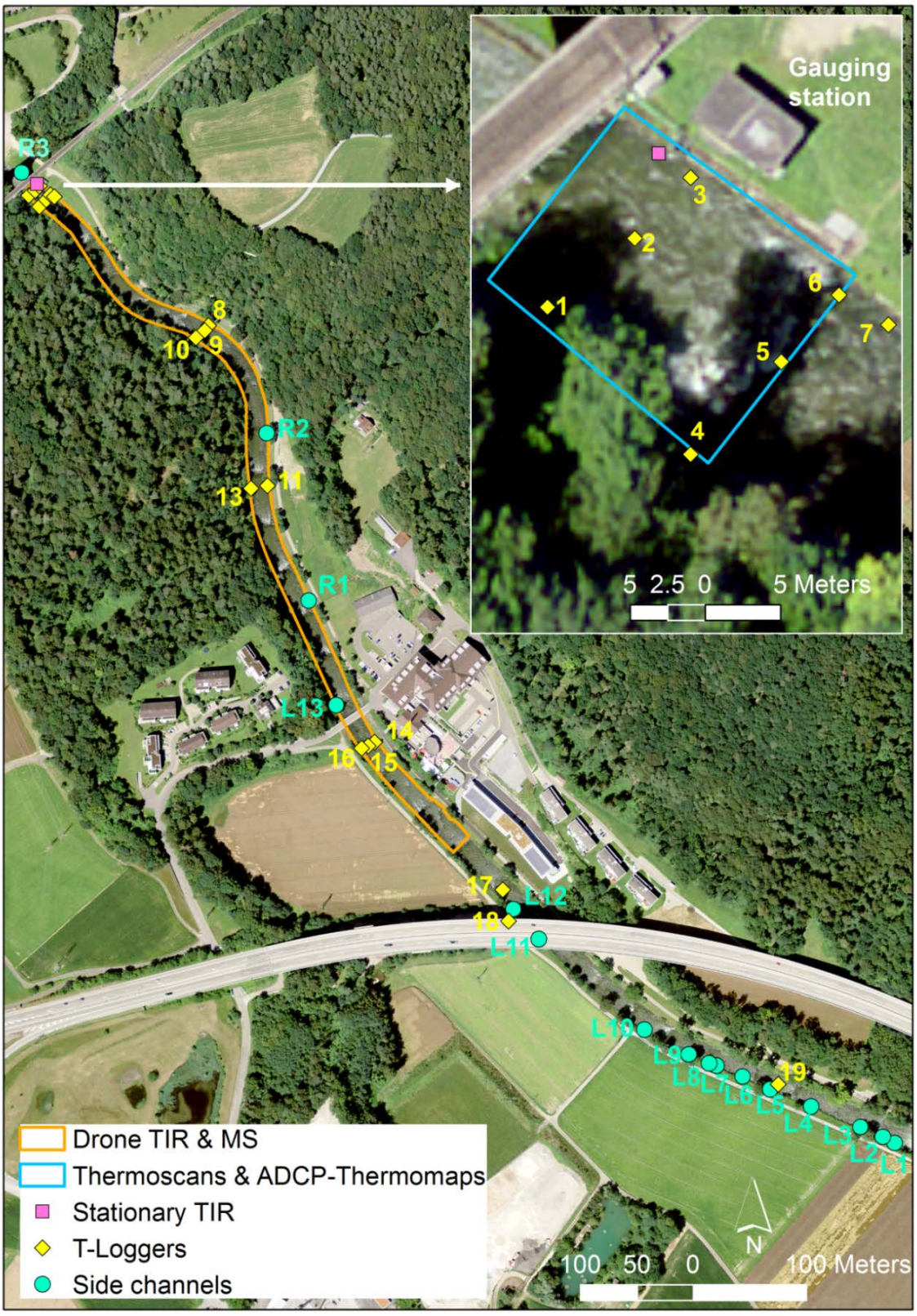

Figure 2. Study reach. Indicated is the perimeter of the analysed drone data (TIR: thermal infrared; MS: multispectral), the drone TIR-thermoscans and thermomaps generated with an Acoustic Doppler Current Profiler (ADCP). The locations of in-situ temperature loggers, side channels and stationary TIR camera are also illustrated. Source background map: Swissimage Geodata © swisstopo.

Thermal infrared (TIR) and multispectral images were remotely collected by drones over three days in order to spatially map continuous surface water temperature patterns and riparian vegetation shading under different meteorological conditions along the Glatt reach (Chap. 3.2). In addition, stationary TIR images were taken at one min intervals over a period of two days to continuously assess surface water temperature (Chap. 3.3.1). Furthermore, temperature loggers were also deployed for approximately one month along and across the entire study reach, to continuously assess water temperature at one min intervals and cross-check remotely sensed water temperature (Chap. 3.3.2). Finally, water temperature was also assessed with an Acoustic Doppler Current Profiler (Chap. 3.3.3).

3.2 High-resolution drone surveys

Approximately 750 m of the study reach were mapped in summer 2018 on two sunny days with clear skies and on one cloudy day in the morning, at noon, and in the afternoon (Tab. 1). Drone flights were scheduled to coincide with minimum (morning) and maximum (afternoon) daily water temperatures and were up to15 minutes long in order to minimize fluctuations in water temperature and shade during the flights. Meteorological conditions for the different dates and flights varied, with higher air and water temperatures but lower air humidity in the afternoon of the two sunny days and almost constant conditions on the cloudy day (Tab. 1). Discharge and water temperature were similar on the two sunny days, while discharge was higher and water temperature lower on the cloudy day (Tab. 1). Sunlight did not reach the gauging station during the morning flights of August 21 and 22 (low solar irradiance in Tab. 1).

Table 1. Characterization of the hydrological and meteorological conditions during the drone surveys. TIR: thermal infrared imagery of the entire reach; MS: multispectral imagery of the entire reach. Hydrological and meteorological data averaged over the respective TIR flight times.

Variables	August 21 2018			August 22 2018			September 2 2018		
	08:21-08:37 MS	12:13-12:25 MS	15:33-15:42 MS						
Time of first and last image & Type of drone survey[A]	08:52-09:03 TIR	12:32-12:43 TIR	15:53-16:04 TIR	08:49-09:00 TIR	12:30-12:41 TIR	15:50-16:01 TIR	09:31-09:41 TIR	13:02-13:13 TIR	15:54-16:06 TIR
	09:08-09:20 MS	12:49-13:02 MS	16:09-16:20 MS	09:04-09:18 MS	13:12-13:25 MS	16:10 16:30 MS	09:49-10:01 MS	13:23-13:39 MS	16:09-16:21 MS
Ground pixel size (m)	MS: 0.09-0.10 TIR: 0.19-0.22								
Discharge (m^3/s)[B]	1.8	2.0	2.0	1.9	2.0	2.0	2.6	2.6	2.6
Water temp. (°C)[C]	19.8	21.7	23.0	19.8	21.9	23.1	16.3	16.7	16.8
Rel. humidity (%)[D]	74.7	45.7	39.2	78.8	49.5	29.5	77.3	71.2	81.4
Wind speed (m/s)[D]	0.0	5.2	5.4	0.0	5.8	2.5	2.5	1.0	0.0
Air temp. (°C)[D]	21.0	29.4	30.8	20.1	29.0	33.1	15.5	16.8	16.6
Global solar irradiance (W/m^2)[E]	70	758	601	62	753	615	115	167	140

[A]Flight start and end times (local time, hh:mm); [B]Recorded at the gauging station; [C]Recorded with logger #3; [D]Recorded at approximately 2 m from ground with a handheld Windmate 300 (WeatherHawk, Logan, UT, USA; accuracy: wind speed and relative humidity ± 3%, air temperature ± 1 °C, manufacturer's specification). [E] Recorded on the roof of the gauging station with a Global-Pyranometer (CPM 11, Kipp & Zonen, Netherland; sensitivity: 7-14 µV/W/m^2, manufacturer's specification; data source: BFH).

3.2.1 Assessment of riparian shading using multispectral images

In order to assess the influence of riparian vegetation shading on the river surface, two kinds of shade were considered (Fig. 3): (i) the shaded area right underneath the overhanging vegetation canopy and (ii) shadows cast by vegetation and topography. The latter can be assessed by directly mapping the shaded areas on the water's surface, whereas the shaded area underneath overhanging vegetation had to be approximated by mapping the area of overhanging high vegetation and assuming that the area covered and therefore shaded by the vegetation remains constant (sun nadir, 100% shaded) during the day. An additional assumption was that if there was no direct sunlight (e.g. no sun, or cloudy), then the area was classified as 100% shaded.

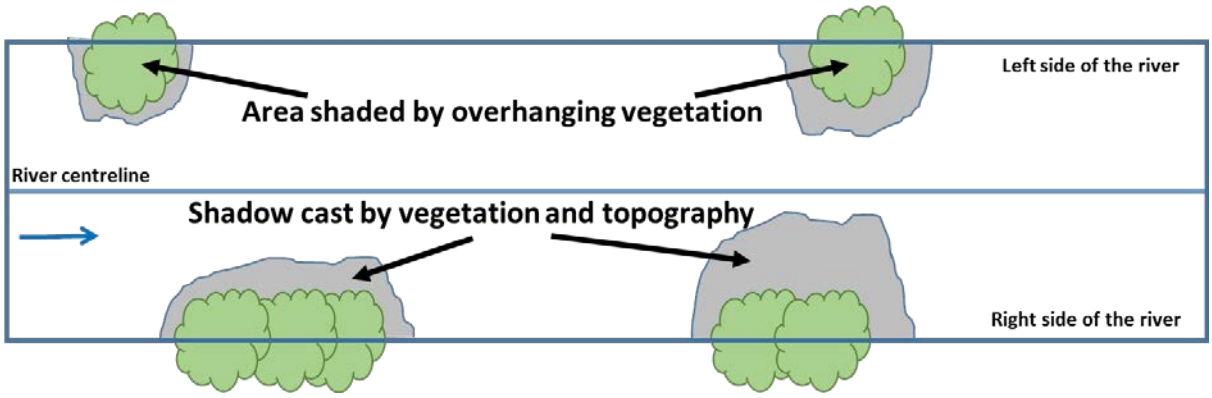

Figure 3: Schematic representation of the two shade types defined in this study.

Multispectral images (five spectral bands; Appendix A) were acquired by the MicaSense RedEdge™ camera mounted on the Wingtra One™ fixed-wing drone. The image datasets were than processed with Pix4D Mapper software (Pix4D 2018). This software relies on automatic feature detection and matching algorithms to retrieve the internal and external orientation of oblique images. Photogrammetric processing derives point clouds, digital elevation models (DEM) and orthoimages of the different bands. 12 ground reference points (GCPs) were used to improve the horizontal accuracy of the generated orthoimages and automated and manual co-registration to a reference dataset ensured optimal alignment (Fig. 4). The accuracy of the imagery co-registration was within two times the pixel size. However, the accuracy was spatially heterogeneous due to distortion effects caused by instable terrain (vegetation canopy) and different numbers of images covering the terrain (generally deteriorating towards the edges). Nevertheless, the data acquisition design guaranteed that the highest possible number of images covered the river, meaning the lowest errors can be expected in this area. The post-processed ground pixel size of the multispectral orthoimages was approximately 10 cm.

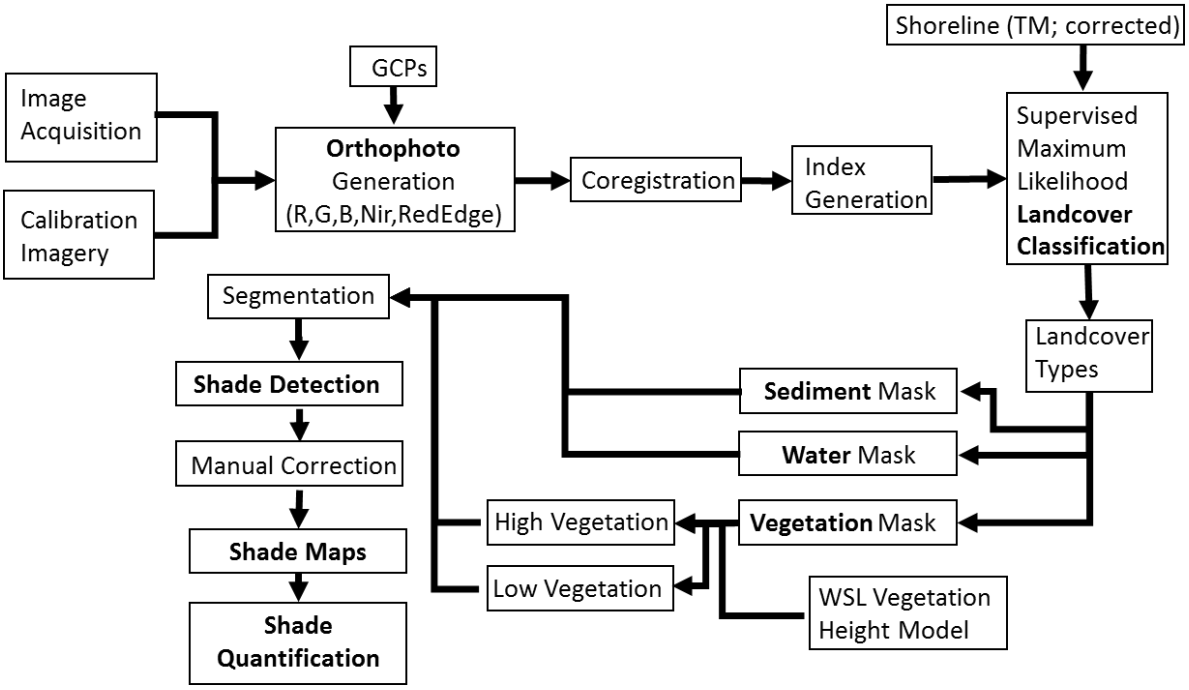

Figure 4. Post-processing workflow for shade assessment using drone multispectral images.

A supervised maximum likelihood landcover classification was applied to the co-registered multispectral data to derive the spatial extent of water, vegetation and sediment (e.g. stones) areas (Fig. 4). Moreover, digital elevation information, the Swiss (WSL) national vegetation height model (Ginzler & Hobi 2015) and manual corrections were applied to increase classification accuracy. Vegetation was further subdivided into high and low overhanging vegetation in order to separate out vegetation that may generate shade.

The acquisition concept was intended to illustrate the spatial dynamic of the shade during the day as well as before and after acquisition of the thermal data (on August 21, Tab. 1). Therefore, the multispectral data was also acquired under non-optimal illumination conditions in the morning and in the late afternoon resulting in weak illumination, low contrasts and a low solar illumination angle. These strongly heterogeneous illumination conditions presented several challenges in relation to processing and analysis of the imagery. Furthermore, the topographical and environmental settings of the study site also posed several challenges in terms of data processing: (i) the dense vegetation canopy complicated detection and matching of image features, (ii) there was restricted space in which to set sufficient GCPs within the study area, (iii) due to the topography, there were some very darkly shaded areas that created saturation effects which influenced the landcover classification and limited automatization efforts. The suboptimal acquisition conditions during the morning and

afternoon flights introduced several artefacts into the data that were manually excluded before analysis (Fig. 4).

Shade Detection & Analysis

Three approaches to automatically identify and map shaded areas were tested: (i) the shade index according to Rikimaru et al. (2002), (ii) shade identification and segmentation based on Ma et al. (2008), (iii) automated shade segmentation based on Polidorio et al. (2003). These three approaches rely on saturation indices, colour intensity and unique brightness as well as colour features of shaded areas. Unfortunately, these approaches did not perform well in the Glatt valley due to the high level of detailed information in the data (high spatial resolution, heterogeneous landcover conditions and visibility of subaequeous structures) and the heterogeneity and peculiarity of the study area that presented variable spectral properties for shaded area. For example, sub-surface aquatic vegetation (macrophytes and algae) in the river have the same spectral signature as shaded areas on the riverbanks and stones, which resulted in misclassifications. Therefore, a manual selection of the segmented imagery combined with the intensity values established by Rikimaru (2002) yielded the best results and was used for the final analysis of shadows cast by vegetation and topography.

The shaded area directly underneath the overhanging vegetation was firstly derived from the Swiss (WSL) national vegetation height model (Ginzler & Hobi 2015) but was found to be of insufficient quality. Therefore, the classified multispectral drone images and the derived digital height model were used to establish which vegetation within the defined river channel was over 2m. This was then classified on the mapped area as high vegetation, resulting in a defined shaded area underneath the overhanging vegetation. This shaded area was assumed to be constant during the all of surveys (100% shaded area).

Finally, in order to quantify the spatial and temporal dynamic of riparian shading on the studied reach of the Glatt River, four different shade properties were calculated and summarized:

i. percentage of overall shadow area cast by vegetation and topography relative to the entire study area;
ii. percentage of shadow area cast from vegetation and topography on the left and right sides of the river (separated by the river centre line, Fig. 3) relative to the entire left and right sides of the study area, respectively;

iii. percentage of shaded area underneath overhanging vegetation (assumed to be constant during the different surveys);

iv. comparison between the shade data derived from the drone based remote sensing and the manually mapped shade transects supplied by the Fischwerk environmental office.

3.2.2 Assessment of water temperature using drone thermal infrared images

Thermal infrared (TIR) images were acquired with a thermomap™ thermal camera (Appendix A) mounted on an ebee classic™ fixed-wing drone system. According to the manufacturer, temperature sensitivity (i.e. the smallest temperature difference that can be detected) is 0.1 °C, accuracy is unknown and the thermal recording range is -40 – +160 °C. The TIR image datasets were processed with Pix4D Mapper software (Pix4D 2018).

Nine distinct topographical features were extracted from the multispectral data and chosen as GCPs in the post-processing workflow (Fig. 5). In addition, tie points were incorporated for automatic and manual co-registration once the TIR orthoimages had been generated. The multispectral data presented in section 3.2.1 was used to produce a water mask that filtered out all vegetation, sediment and mixed pixels in order to assure that only pure water pixels were used in further analysis (Fig. 5).

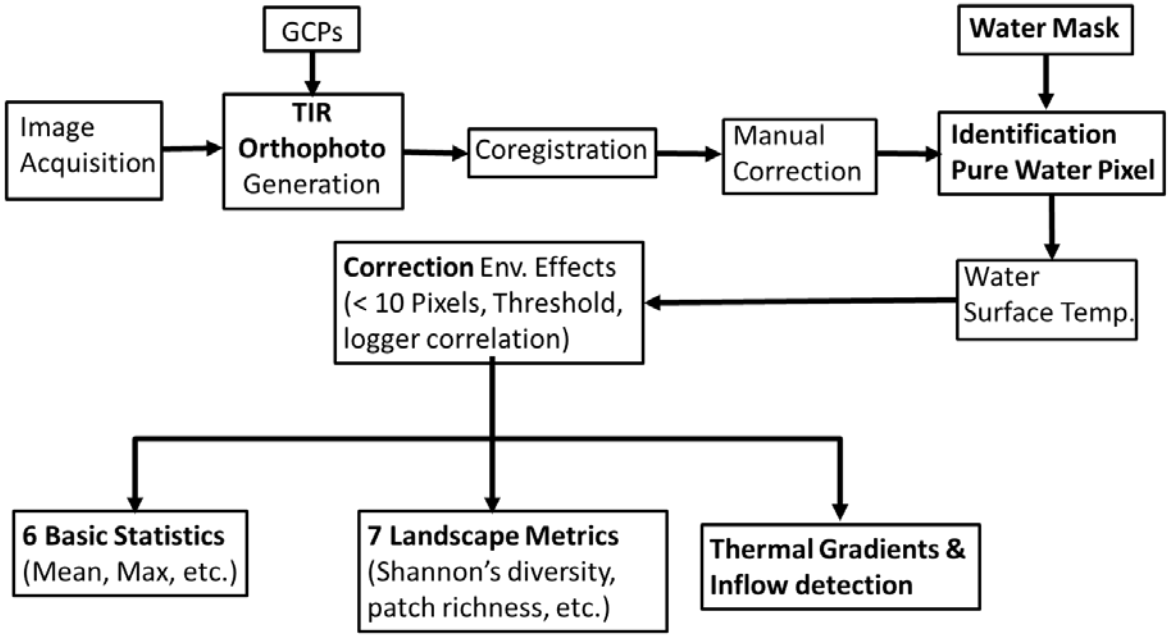

Figure 5. Post-processing workflow for temperature assessment using drone TIR images.

Illumination effects resulting from the topography, the optical permeability of the shallow water and the general heterogeneity of the different landcover classes posed difficulties in the classification of vegetation and sediment. For example, algae and macrophythes were detectable on the riverbed and were classified as vegetation even though they were totally submerged (Appendix B). Therefore, an aggressive filtering of water pixels was necessary in order to ensure reliable analysis of the actual water area. This approach resulted in an underestimation of the actual water area but minimized errors resulting from misclassification (sub-pixel mixing). The co-registered and water masked TIR orthoimages were then used to provide surface water temperature data (T_r: radiant temperature; radiant temperature is equivalent to the emitted energy of an object) with a high spatial resolution. The post-processed ground pixel size of the TIR orthoimages was approximately 20 cm.

In addition to the TIR images collected over the entire study reach with the drone, so-called thermoscans of the area between two artificial weirs in front of the gauging station (Fig. 2) were performed on August 12 (11:00 – 12:00; sunny) and September 2 (11:00 – 12:30; cloudy) at approximately 60 min and 30 min intervals, respectively.

Analysis

The drone TIR orthoimages were analysed using R software version 3.5.1 (R Core Team 2018). First, mosaics were converted from ESRI Geodatabase Raster Datasets to TIFF images, in order to guarantee readability in R while keeping the file size. Second, four correction steps were performed before analysing the TIR orthoimages (Fig. 5):

i. based on the thermal camera sensitivity, temperatures were rounded to one decimal point;
ii. small temperature classes (i.e. < 10 pixels) were not considered representative and therefore discarded;
iii. pixels with a T_r above a certain threshold were discarded because they were clearly not water pixels or contained artefacts. The threshold was set as the mean T_k of all the orthoimages plus 1 °C and then rounded;
iv. to account for atmospheric and other environmental effects, T_r values were corrected assuming a linear relationship between T_r and T_k (Lebourgeois et al. 2008; Lee et al. 2016). T_r was calculated by averaging all water TIR pixels that fell within a circular region (radius set to 0.5 m, ca. two TIR-pixels, to account for the inaccuracy of the RTK-GPS

receiver and the TIR orthoimages) around the location of the temperature loggers. The T_k measured by the *in-situ* temperature loggers was calculated as the average temperature throughout the duration of the TIR flights.

The following statistics (Fig. 5) were then calculated for each corrected drone TIR orthoimage using the "raster" (Hijmans 2017) and the "SDMTools" packages (VanDerWal et al. 2014):

i. six basic thermal statistics: number of pixels, mean, standard deviation, min. and max. temperature, temperature amplitude;
ii. seven landscape metrics according to Faye et al. (2016):
    - three diversity metrics: thermal patch richness (number of temperature classes present in the thermal mosaic), Simpson's thermal diversity index (indicates the probability that two pixels selected randomly would belong to different temperature classes), Shannon's thermal diversity index (quantifies the uncertainty in predicting the temperature of one pixel that is chosen randomly in the thermal mosaic);
    - two aggregation metrics: thermal aggregation index (quantifies to what extent pixels of the same temperature class are spatially aggregated), thermal cohesion index (quantifies the physical connectedness between patches of the same temperature);
    - one shape metric: thermal landscape shape index (standardized measure of the total edge of a given thermal class);
    - One subdivision metric: thermal patch density (number of patches per unit area).

Thermal gradients along the river centreline and two longitudinal profiles set at four meters parallel to the centreline were also investigated by extracting the temperature values for pixels spaced 10 meters apart that fell on the corresponding lines (Fig. 6). The centreline was derived using a tailored toolbox in ArcMap and the two parallel lines were generated by applying a buffer around the centreline. To investigate temperature variations within cross sections perpendicular to the approximately 750 m long reach and to detect potential cold-water inflows, 72 transects spaced at 10 meter intervals were defined (Fig. 6). For each of the transects, the pixels from the TIR orthoimage that fell on the cross-section lines were extracted and used to draw boxplots and levelplots. A further approach used to detect inflows was a "change point" analysis that was performed using the "changepoint" package (Killick & Eckley 2014). This analysis allows points where statistical properties change (e.g. mean and standard deviation) to be identified within a dataset (Fricke & Baschek 2015).

Finally, the cold patch detection approach introduced by Wawrzyniak et al. (2016) was employed, in which the median water temperature within a five-meter buffer around the river centreline was calculated and then the areas with a temperature at least 0.5 °C colder than this value were defined as cold-water patches (Fig. 6).

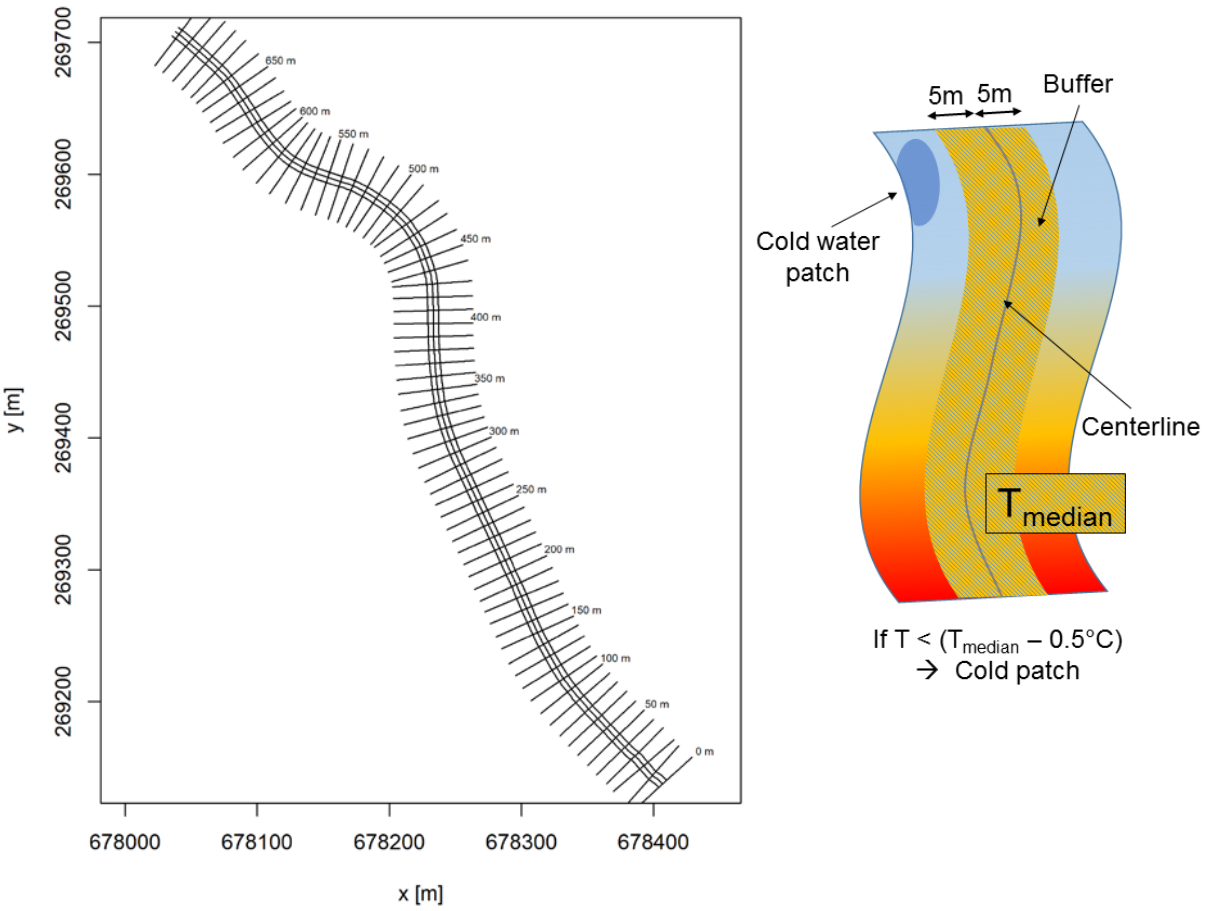

Figure 6. Left: Example of centreline, left and right side river lines, and cross sections for the analysis of thermal gradients and inflow detection. Flow direction is from bottom to top. Right: Schematic representation of the cold patch detection approach introduced by Wawrzyniak et al. (2016).

3.3 In-situ measurements

3.3.1 Assessment of water temperature using a stationary thermal infrared camera

Stationary thermal infrared (TIR) images were continuously recorded at one min intervals on August 12 (07:50-16:50; sunny) and September 2 (08:50-16:10; cloudy) using a FLIR t620 thermal camera (FLIR Systems Inc., Wilsonville, OR, USA) vertically (nadir) mounted on a wooden bar located approximately three meters above the water's surface and 1.5 meters from the right river bank near the gauging station (Fig. 2). According to the manufacturer,

temperature sensitivity is < 0.04 °C, measurement accuracy ±2 °C (± 2 %) and thermal recording range -40 – +650 °C.

TIR images from the stationary camera were analysed by extracting the radiant surface water temperature of the pixel located in the middle of each image (centre spot) and comparing this with the water temperature recorded by the closest logger (#3, Fig. 2).

3.3.2 Assessment of water temperature using temperature loggers

The kinetic water temperature (T_k; kinetic temperature is the contact heat energy of an object) was continuously recorded at one min intervals using Vemco Minilogg II temperature loggers (AMIRIX Systems Inc., Halifax, NS, Canada; temperature range −30 to 80 °C, resolution 0.01 °C, accuracy ±0.1 °C, manufacturer's specification). In total, 19 loggers were placed in protective stainless-steel cases, which have minimal influence on instantaneous temperatures (±0.1 °C; Malard et al. 2001), and deployed over the entire study reach (Fig. 2). The recording period lasted for approximately one month, from August 7 at 23:47 until September 2 at 16:13. Two loggers were either lost due to a small flood event on August 14 (ca. 20.5 m^3/s) or to human intervention. One logger (#2) was replaced on August 17 (resulting in 37% of the data being lost), the other logger (#12) was not replaced (Fig. 2). After the sampling period, the loggers' inter-accuracy was checked in a temperature-controlled water bath. The average temperature across all the loggers (n=18, 6h, 1-min interval) was calculated and then the maximum temperature difference determined for each individual logger. Maximal differences ranged from +0.17 °C to -0.09 °C (Appendix C, Tab. C1).

Analysis

The T_k values recorded with the loggers were used to characterize the temporal dynamic of the water temperature along and across the reach. Moreover, they were used to validate and correct the radiant surface water temperature (T_r) that had been estimated by means of infrared thermography (Chap. 3.2.2).

The temporal dynamic of the water temperature was investigated using six thermal variables calculated for the T_k from each temperature logger over the entire sampling period (for calculations see Arscott et al., 2001): (i) minimum T_k, (ii) maximum T_k, (iii) average T_k, (iv) T_k pulse (amplitude; i.e. the difference between maximum and minimum T_k), (v) maximum

kinetic rate of thermal heating (maximum temperature difference per hour), and (vi) maximum kinetic rate of thermal cooling (minimum temperature difference per hour). In addition, three temperature-related metrics of specific relevance to fish were also calculated (for calculations see Wolter, 2007): (vii) cumulative kinetic degree-days (cumulative sum temperature of the average daily temperatures over the sampling period), (viii) cumulative kinetic degree-days above 24 °C, and cumulative kinetic degree-days below 20 °C. In order to calculate the degree-day variables, days with no complete data (i.e. full days) were eliminated for all loggers; as a result 25 days out of 27 days were used for these calculations. As already stated above, 37% of the data from logger #2 was lost (10 days). Thus, results from this logger could not be directly compared with the other loggers.

Thermal stratification and side channels

During the surveys no significant thermal stratification was found (T_s = 0.0 ± 0.01 °C, max. T_s = 0.2 °C) (Appendix C, Tab. C2). Thus, the T_k recorded by the loggers can be considered to be indicative of the overall water column temperature and consequently be used for validation and correction of the radiant surface water temperature (T_r) estimated by means of infrared thermography.

The temperatures of the 16 side channels found during the field survey (Fig. 2) ranged between 12.6 and 16.1 °C and the average temperature for all of the side channels was 14.7 ± 0.9 °C (Appendix C, Tab. C3). These channels are most probably groundwater-fed and could have an influence on the water temperature of the Glatt River. Logger #18 was located in a 3rd order side channel that delivered, by far, the largest discharge (ca. 65 L/s in August-September; FOEN 2018c), all the other side channels discharged very little water or were dry on the survey dates.

3.3.3 ADCP-Thermomaps

Parallel to the drone TIR thermoscans (Chap. 3.2.2), kinetic water temperature (T_k) was continuously recorded at one sec intervals in the area between two artificial weirs in front of the gauging station (Fig. 2) using a SonTek M9 Acoustic Doppler Current Profiler (ADCP, San Diego, CA USA; temperature range −5 to 45 °C, resolution 0.01 °C, accuracy ±0.1 °C, manufacturer's specification) that was mounted on a SonTek Hydroboard II and coupled and synchronized with a differential GPS (sub-meter position accuracy). Data was collected on

August 12 (11:00 – 13:00; sunny) and September 2 (11:15 – 13:15; cloudy) at approximately 15 min and 30 min intervals, respectively. The ADCP-thermomaps were evaluated to see if they could be used to measure spatio-temporal changes in water temperature.

4 Results

4.1 Assessment of riparian shading using multispectral images

4.1.1 Spatio-temporal quantification of shade distribution and dynamics

The high-resolution multispectral drone based data allowed the spatial distribution of shade on the river surface and the spatio-temporal dynamic of shade coverage to be quantified. On August 21 the shadow cast by vegetation and topography ranged from 83% of the entire study area at 08:21 to 17% at 12:13 (Fig. 7 "All"). Shaded areas directly underneath the overhanging vegetation canopy contributed only a very small amount to the total shaded area (ca. 9%; Fig. 7 "Vegetation All"). Similar trends were also detected on August 22 (Appendix D). Therefore, the general topographical setting as well as the structure and height of the riparian vegetation played a far more important role in determining the shaded area of the study site. The diurnal shadow evolution on the left and right sides of the river followed the path of the sun over the horizon. As the general orientation of the study site is N-S, more shadows were cast in the morning on the right/eastern side of the river, whereas in the afternoon more shadows were cast on the left/western side of the river (Fig. 7 "left", "right"). It should be noted that in the morning (08:21 vs 09:08) and in the afternoon (15:33 vs 16:09) there was only an approximate 40 min timespan between the datasets, but the shaded area generated by the vegetation canopy changed by approximately 15% in the morning and 7% in the afternoon (Fig. 7 "All").

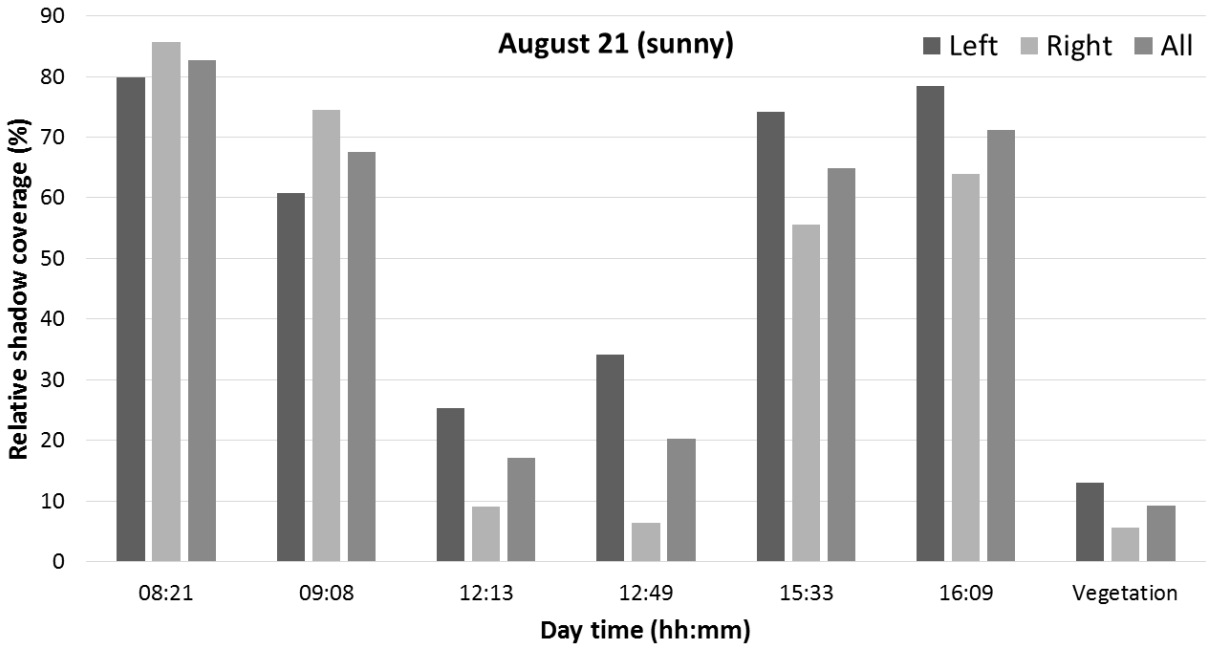

Figure 7. Percentage coverage of oblique shadows cast by vegetation and topography on the left and right sides of the rivers and the entire study area ("all"), and percentage coverage of the shaded area underneath the overhanging vegetation ("vegetation") on August 21 (see Fig. 3). Percentages relative to area covered.

Figure 8 shows an example of the evolution of shade dynamics on one selected section of the study reach. In the morning, at approximately 08:20, the local topography and vegetation cast a shadow over the entire river (Fig. 8a). Approximately 45 min later, the sun had already reached the river's surface, thus reducing the shaded area (Fig. 8b). As expected, the lowest shade coverage was detected around noon (Fig. 8c) when the sun was almost perpendicular to the river's surface. However, within approximately 35 minutes the shaded area had already changed (Fig. 8d). In the afternoon, the river was again almost completely in shade (Figs. 8e & 8f).

The temporally dense shade datasets from August 21 clearly show that shade coverage is highly dependent on topography and vegetation, and that considerable changes can occur very quickly (Figs. 7 & 8).

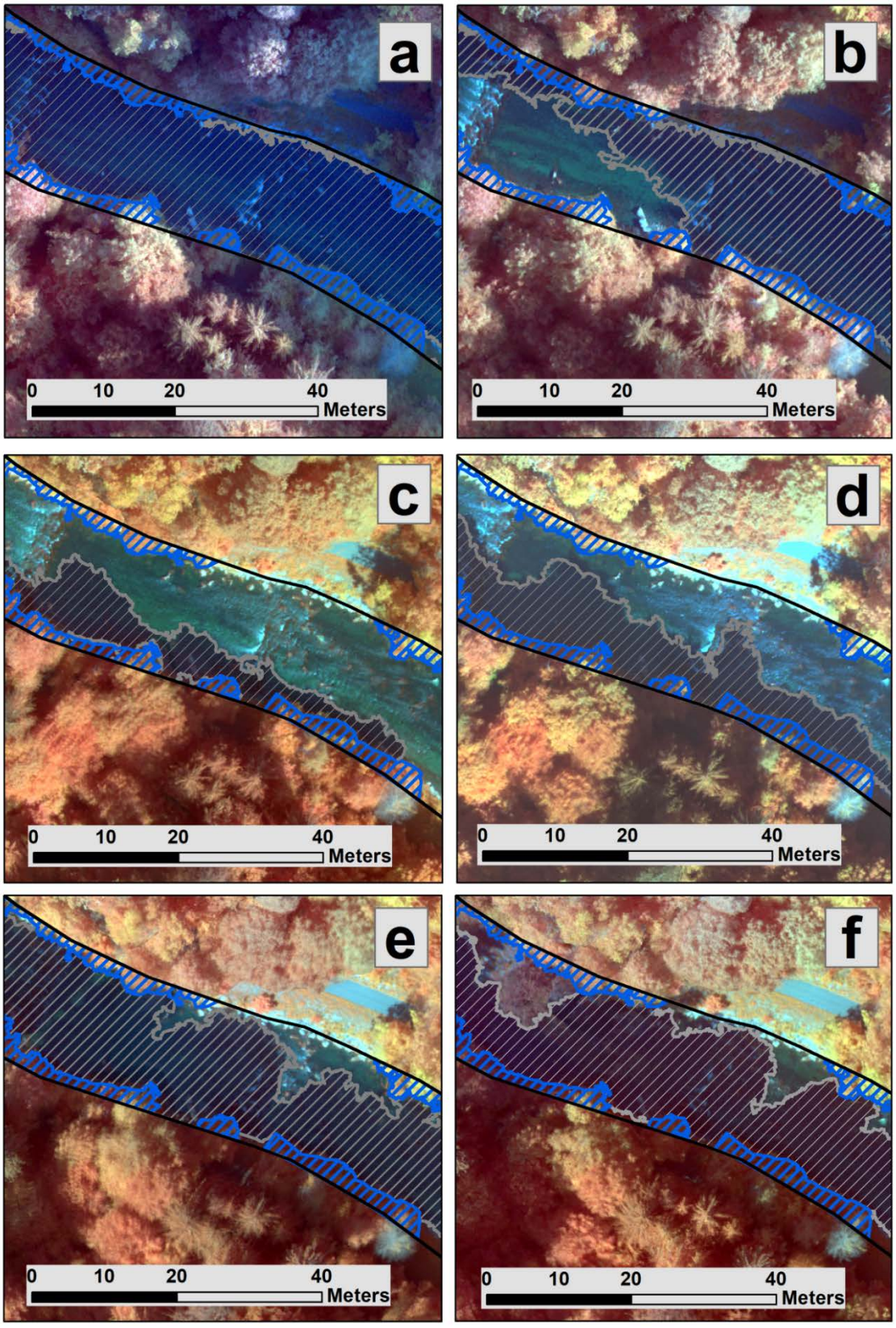

Figure 8. Results of the shade classification at different times on August 21 (sunny) on one selected section of the Glatt river. The grey area shows the oblique shadows cast by vegetation and topography and the blue area show the shaded area underneath the overhanging vegetation. The combination results in the total shaded area. The results show the survey times: a) 08.21, b) 09:08, c) 012:13, d) 12:49, e) 15:33, f) 16:09. Flow direction is from right to left. Background maps: NirGB orthoimages from August 21. It should be noted that the artefact introduced by increasing wind during the afternoon in the NW part of Fig. 8f was manually excluded before final analysis.

4.1.2 Drone shade quantification vs manually mapped shade

Manual field observations were conducted by the Fischwerk environmental office to map the shade on the study area around 10 days before the drone data acquisition. During this field survey, the shaded area of the entire river each was divided into four categories by visually estimating stretches of homogeneous shade coverage along the river at three times of the day (morning 08:39-09:48, noon 12:10-12:48, afternoon 15:21-16:23). The shade categories were 0-25%, 25-50%, 50-75% and 75-100%.

Good agreement between the manually estimated sahde coverage and the shaded areas quantified from the multispectral drone data could be found (Fig. 9). The local differences were mostly small and mainly the result of a few percentage discrepancies between the multispectral derived sahde and the manually estimated ones, which resulted in a different (higher or lower) category. Although, Figures 7 and 8 clearly showed how quickly the shaded areas can change within a short time-span. Therefore, because the drone data acquisition took around 12 minutes and the manually conducted field surveys lasted around one hour, it can be expected that the uncertainty of the shaded area mapped by the drone is lower than for the manual approach.

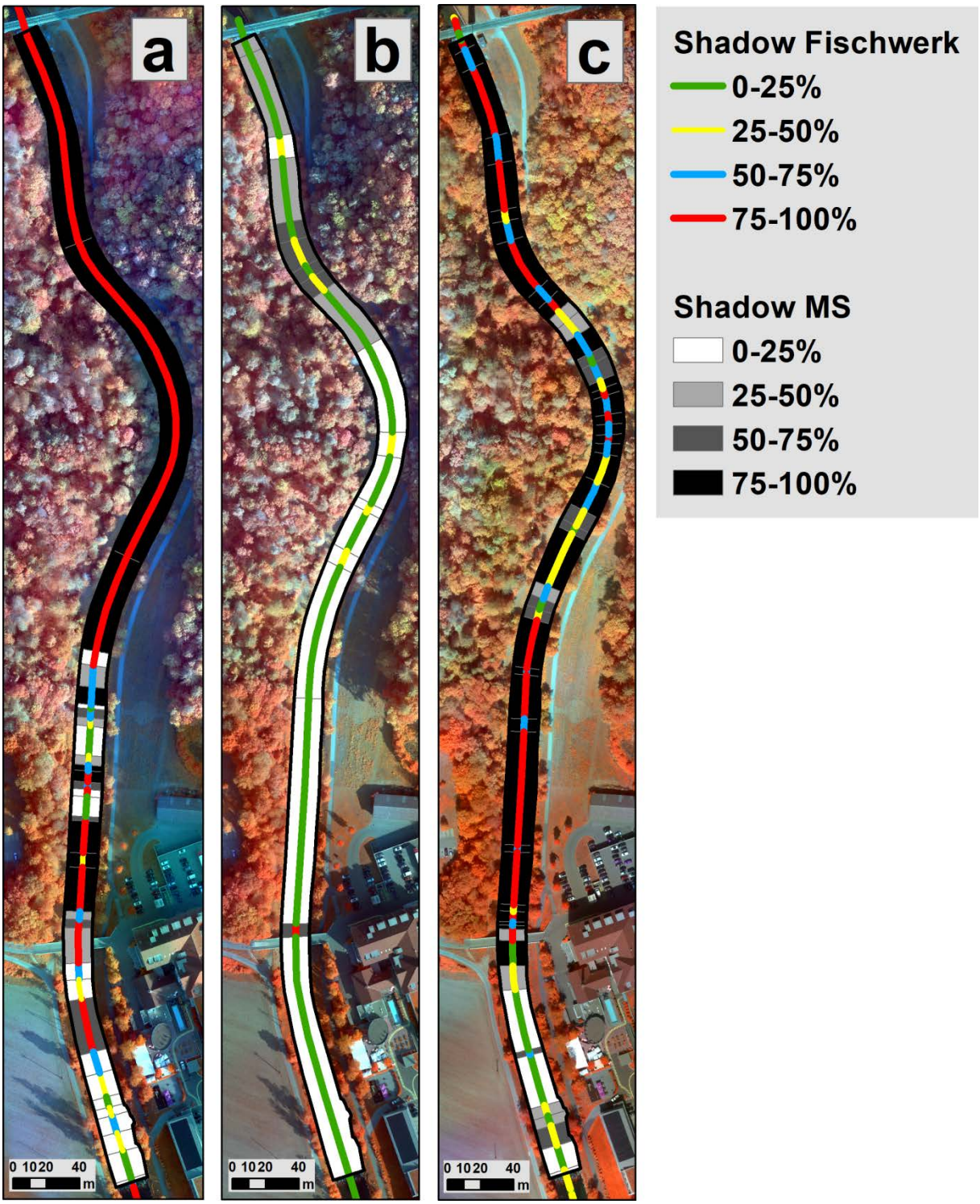

Figure 9. Comparison of the shade coverage derived from drone remote sensing (MS: multispectral orthoimages) and from manual mapping in the field (Fischwerk data): a) morning, b) noon c) afternoon. The line in the middle of the channel visualizes the ratio of shade (%) within that area of the river from the Fischwerk acquisition, and the underlying greyscale areas show the shade ratio (%) in the same areas derived from the drone based data. Drone images were acquired on August 21 at 09:08-09:20, 12:13-12:25 and 15:33-15:42. Flow direction is from bottom to top. Background maps: NirGB orthoimages from August 21.

4.2 Assessment of water temperature

4.2.1 Validation and correction of surface water radiant temperature

Drone TIR derived radiant temperatures (T_r) can be overestimated (noon and afternoon) or underestimated (morning) compared to *in-situ* T_k measurements (Table 2). The highest overestimations were reported for August 22 when T_r was 5.1±0.4 °C warmer on average than T_k. After correction, to account for atmospheric and other environmental effects, the mean differences between T_r and T_k were considerably reduced to 0.0/0.1 ± 0.1/0.2 °C. However, some local differences of up to 0.5 °C remained (Tab. 2).

Table 2.Comparison between T_r and T_k. T_k: kinetic temperature measured by in-situ temperature loggers; T_r: radiant temperature derived from the drone TIR images. Corrected: T_r corrected assuming a linear relationship between T_r and T_k (Lebourgeois et al. 2008; Lee et al. 2016). Only loggers located in the centre of the river (# 2, 5, 9, 15; Fig. 2) were used to build this relationship because the water in the centre is expected to be better mixed due to turbulence and active vertical exchange than near the river banks and because environmental effects that might affect T_r are normally less pronounced in the centre of the river. Min, max, mean and SD (standard deviation) were calculated using data from all of the loggers except for loggers #1 and #16.

Date	Day time	$T_r - T_k$ raw			$T_r - T_k$ corrected		
		Min	Max	Mean ± SD	Min	Max	Mean ± SD
21 August 2018	Morning	-0.3	0.8	0.1 ± 0.3	-0.3	0.0	-0.1 ± 0.1
	Noon	2.4	4.0	3.2 ± 0.4	-0.1	0.2	0.0 ± 0.1
	Afternoon	3.6	5.0	4.2 ± 0.4	-0.1	0.3	0.1 ± 0.1
22 August 2018	Morning	-0.3	0.3	0.1 ± 0.2	-0.3	0.0	-0.1 ± 0.1
	Noon	3.0	3.9	3.5 ± 0.3	-0.1	0.2	0.0 ± 0.1
	Afternoon	4.4	6.0	5.1 ± 0.4	-0.1	0.5	0.1 ± 0.2
2 September 2018	Morning	-1.3	0.0	-0.9 ± 0.5	-0.3	0.0	0.0 ± 0.1
	Noon	0.2	0.5	0.3 ± 0.1	-0.2	0.1	0.0 ± 0.1
	Afternoon	0.0	0.6	0.2 ± 0.2	-0.1	0.1	0.0 ± 0.0

4.2.2 Quantification of the temporal thermal dynamic of the water using *in-situ* loggers

Over the entire reach, the T_k of all of the loggers, except #18, recorded a similar temporal temperature dynamic (Fig. 10; Appendix E). T_k ranged from a minimum of 16.0 °C (logger #16) to a maximum of 24.2 °C (loggers #11 & #14), while the average temperature ranged from 19.9 ± 1.7 °C (logger #16) to 20.4 ± 1.9 °C (logger #14) during the recording period. Logger #10, which was located in a shallow standing pool (Appendix C, Table C2), recorded the highest rate of thermal heating (1.4 °C/h; Appendix E). However, Logger #18 recorded a completely different temporal temperature dynamic, with a much lower average temperature (16.1 ± 0.7 °C), a reduced temperature amplitude (6 °C) and much higher rates of thermal

heating and cooling (3.2 & -1.7 °C, respectively) (Fig. 10; Appendix E). This logger was located in a 3rd order side channel on the left side of the river, which is probably fed by cold ground-water. No clear thermal gradient from upstream to downstream or clear difference between loggers located on the left or right sides of the river could be detected (Fig. 10).

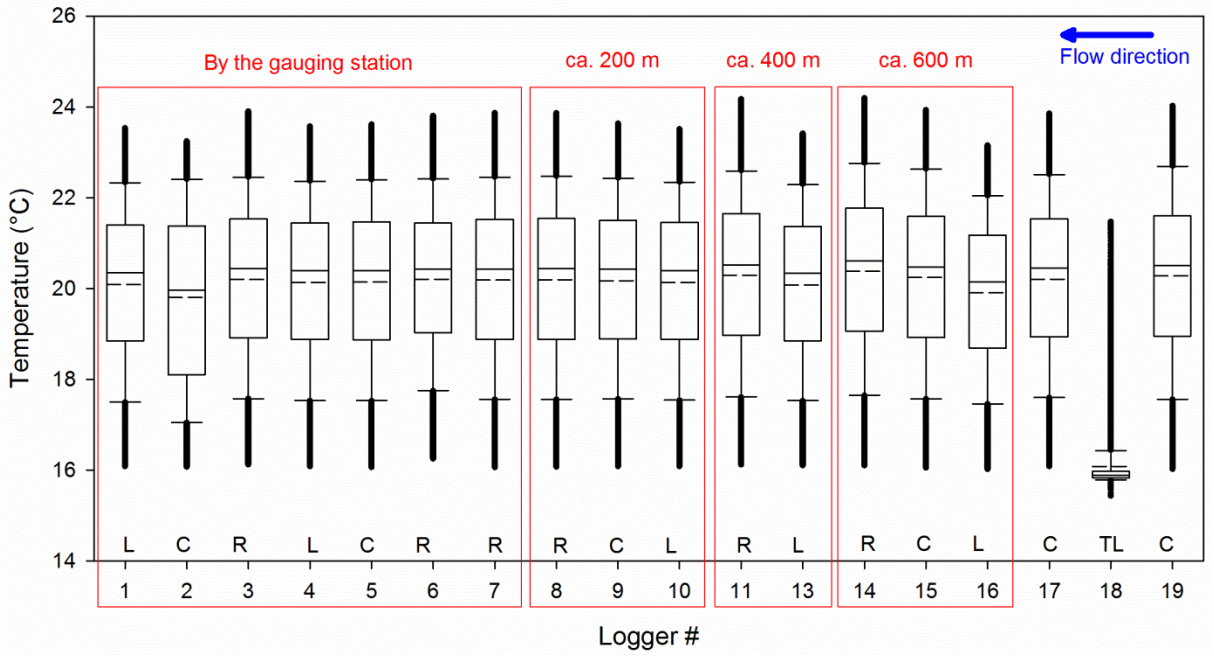

Figure 10. Characterization of the temporal dynamic of the water temperature (°C) recorded by each in-situ logger located on the left (L), in the centre (C) and on the right (R) of the river, and in a 3rd order side channel on the left of the river (TL; logger #18). See Figure 2 for the logger locations. Recording period lasted from August 7 at 23:47 until September 2 at 16:13. Logger #12 was either lost as the result of a small flood event on August 14 (ca. 20.5 m3/s) or due to human intervention. Logger #2 was replaced on August 17, resulting in a loss of 37% of the data. Boxplots show the 25th and 75th percentiles, median (straight line in the box), mean (dashed line), whiskers (90th and 10th percentiles) and outliers (black dots).

4.2.3 Quantification of the temporal thermal dynamic of the water using a stationary thermal infrared camera

The TIR radiant temperatures (T_r) measured by a stationary camera correlated very well with the *in-situ* logger T_k measurements ($0.80 < r^2 < 0.99$; Fig. 11). On the sunny day, T_r was lower than T_k (mean: -0.64 ± 0.19 °C; range: -0.12 – -1.18 °C), whereas on the cloudy days T_r was slightly higher than T_k (mean: 0.13 ± 0.10 °C; range: -0.15 – 0.45 °C). This was probably due to the differences between water temperature and air temperature (difference between sunny and cloudy days) that have an impact on atmospheric emissions and absorption and thus may induce an overestimation or underestimation of T_r.

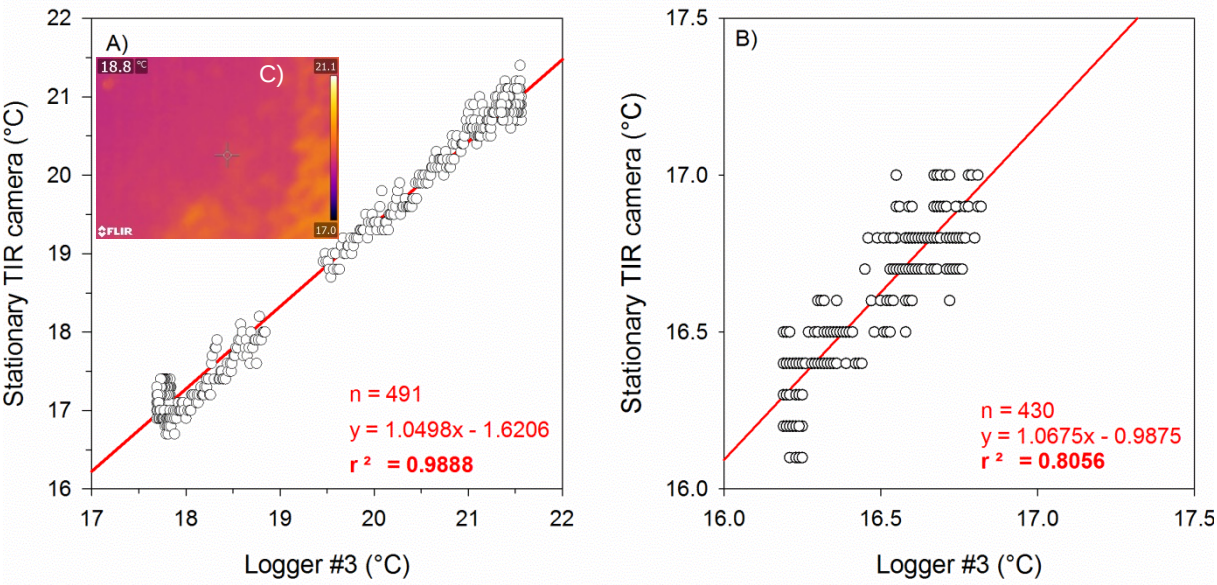

Figure 11. Comparison between radiant temperature (T_r) from a stationary TIR camera and kinetic temperature (T_k) measured by in-situ temperature logger #3 on A) August 12 (07:50-16:50; sunny) and B) September 2 (08:50-16:10; cloudy). C) Example of stationary TIR image with spot (cross) T_r measurement (August 12 at 12:02). Battery failure and/or replacement resulted in 9.2% and 2.5% of the data being lost for A) and B), respectively. Please note different x- and y-axes scales. See Figure 2 for location of logger #3 and stationary TIR camera.

4.2.4 Quantification of the spatial thermal dynamic of the water using drone thermal infrared images

The high resolution TIR drone data allowed the spatial distribution and dynamic of thermal patterns to be quantified. A distinct daily variation in radiant surface water temperatures was detected on the two sunny days, whereas the temperature was more uniform on the cloudy day (Figs. 12-16; Appendix F, Figs. F1-F4). From morning to afternoon of the sunny day on August 21, the average surface temperature and temperature amplitude over the entire reach increased by 3.2 °C and 0.4 °C, respectively (Fig. 13). Whereas, on the cloudy day on September 2, the average surface temperature and temperature amplitude over the entire reach were relatively uniform and increased by only 0.6 °C and 0.1 °C, respectively (Fig. 13). The temperature distribution over the entire study reach was almost uniform, with temperature differences (amplitude) between a minimum of 0.0 °C (morning of September 2) and a maximum of 0.7 °C (afternoon of August 21) (Figs. 12 & 13).

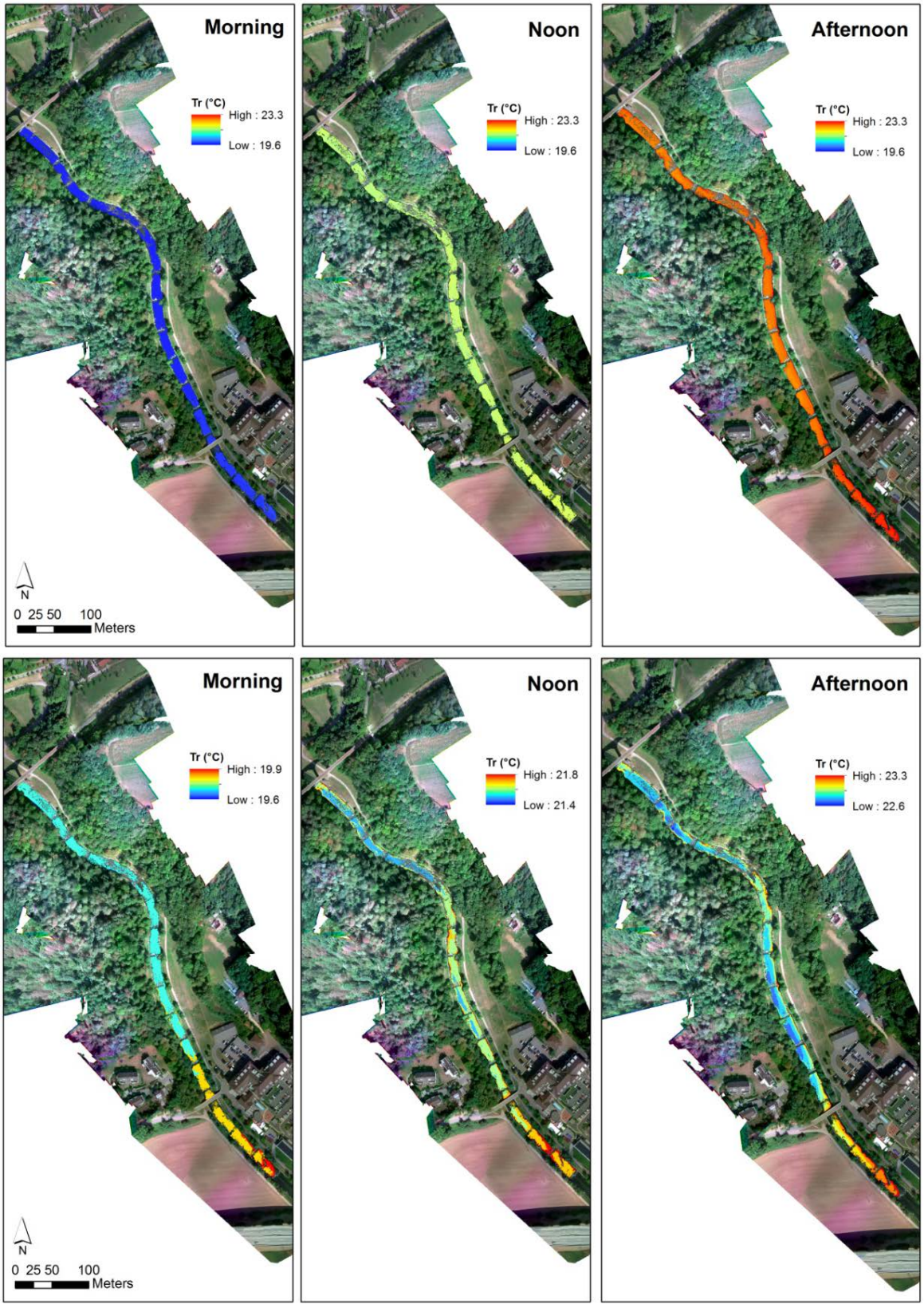

Figure 12. Temperature corrected TIR orthoimages (spatial distribution of radiant temperature (T_r) values per pixel) of the entire study reach in the morning, noon and afternoon of August 21. Note that for the top three images, the temperature scale was kept constant (19.6 – 23.3 °C) for all three periods of the day, whereas for the bottom three images each period of the day is represented with the exact temperature range (thus showing more temperature differences; however most of these differences lie within the possible image error range of ± 0.5 °C). See Table 1 for exact flight times. Flow direction is from south to north. Background maps: RGB orthoimages of August 21.

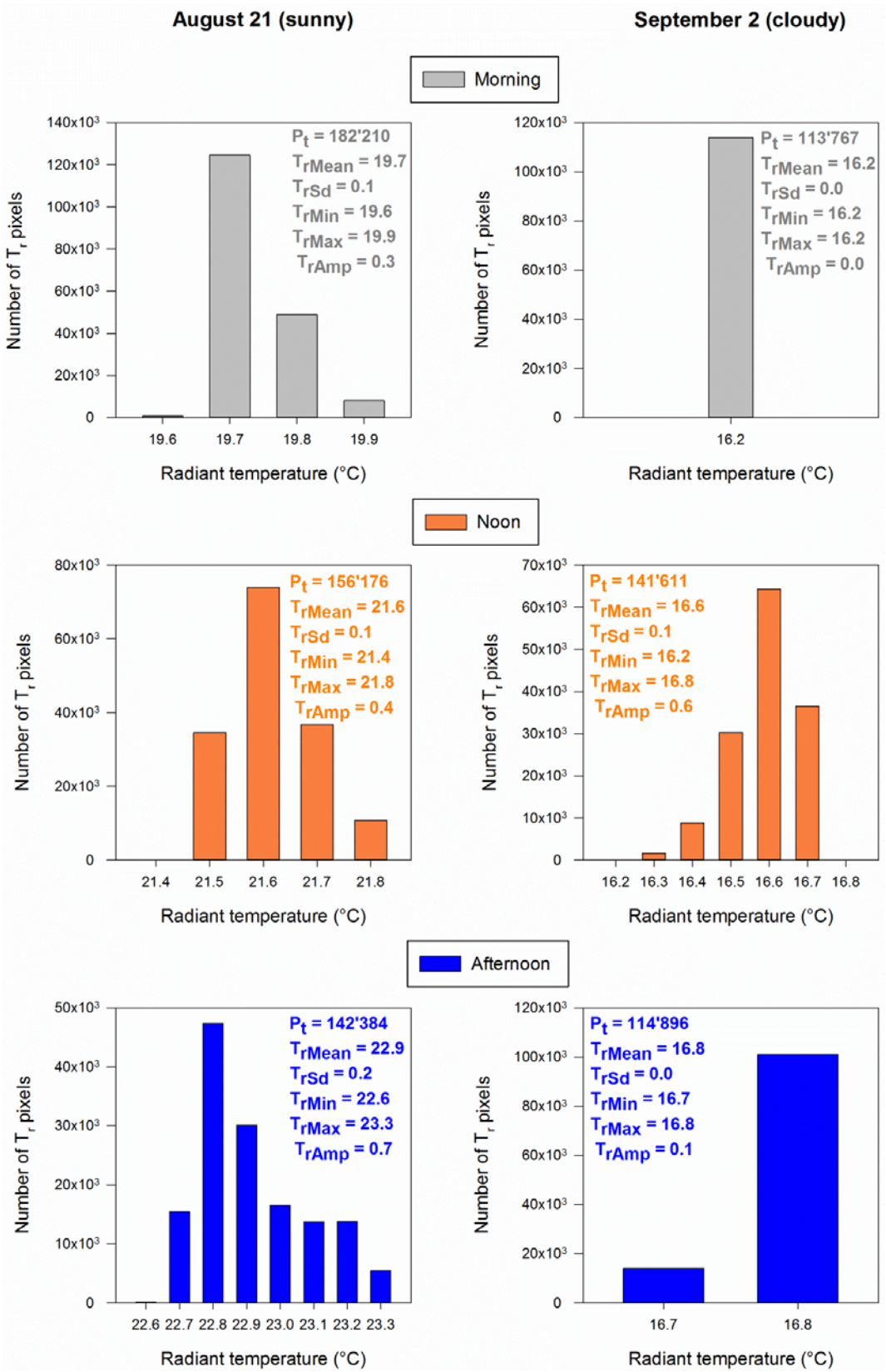

Figure 13. Pixel frequency distribution of corrected radiant temperature (T_r) over the entire study reach in the morning, at noon and in the afternoon of August 21 (sunny) and September 2 (cloudy). Statistics for each histogram include six basic statistics: total number of pixels (P_t), mean radiant temperature (T_{rMean}), standard deviation of radiant temperature, (T_{rSd}), minimum radiant temperature (T_{rMin}), maximum radiant temperature (T_{rMax}) and radiant temperature amplitude (T_{rAmp}). Please note the different x- and y-axes scales. See Table 1 for exact flight times and Figures 12 & F1 (appendix F) for corresponding TIR orthoimages.

Some slightly warmer areas were detected at the start of the study reach on all three survey days (Fig. 12 bottom & Fig. 14; Appendix F, Figs. F1, F3 & F4). Analysis of the centreline data showed some correlation between downstream distance and decreasing temperature on the two sunny days ($0.22 \leq r^2 \leq 0.69$). Moreover, temperature variability within the cross sections increased from morning to afternoon (box amplitude in Fig. 14), which was further influenced by the number of temperature pixels on each cross-section. The downstream longitudinal gradient might also have been influenced by the wastewater treatment plant located approximately 450 m upstream of the start of the reach. However, this trend was not confirmed by the *in-situ* measurements (Fig. 10) and most differences were within the possible TIR image error range of ± 0.5 °C (Tab. 2). Therefore, no longitudinal downstream cooling effect could be confirmed.

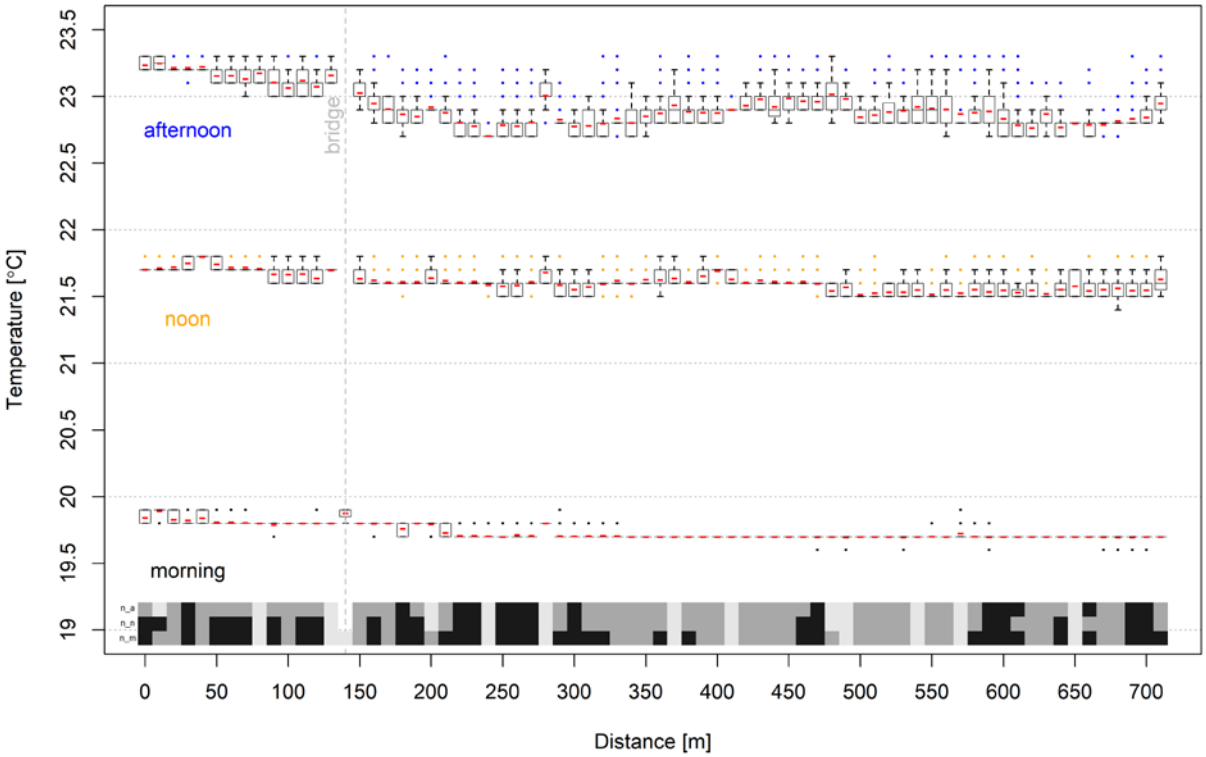

Figure 14. Corrected thermal gradients of the radiant surface temperature (T_r) of the entire study reach in the morning, at noon and in the afternoon of August 21. Boxplots represent temperature variations in 72 cross sections (spaced by 10 m) perpendicular to the ca. 750 m long reach. Boxplots show the 25th and 75th percentiles, median (black line in the box), mean (red line in the box), whiskers (25th - 1.5 x IQR; 75th + IQR) and outliers (dots). Grey-black boxes on the x-axis show the total number of pixels (n) in each boxplot (the darker the colour, the higher the "n" value) with n_a: afternoon, n_n: noon, n_m: morning. Flow direction is from left to right. See Table 1 for exact flight times and Figure 12 for corresponding TIR orthoimages.

The calculated landscape metrics depicted similar spatial heterogeneity in radiant surface water temperature on the two sunny days, while on the cloudy day different patterns were observed (Fig. 15). In general, the temperature pixels were more spatially aggregated and connected (AI and CI) on the cloudy day, whereas the thermal landscapes on the sunny days had greater temperature diversity (PR, SIDI and SHDI), especially in the morning and in the afternoon. This spatial temperature heterogeneity was probably increased by the higher air temperature and greater ambient effects (e.g. shadow) on the sunny day.

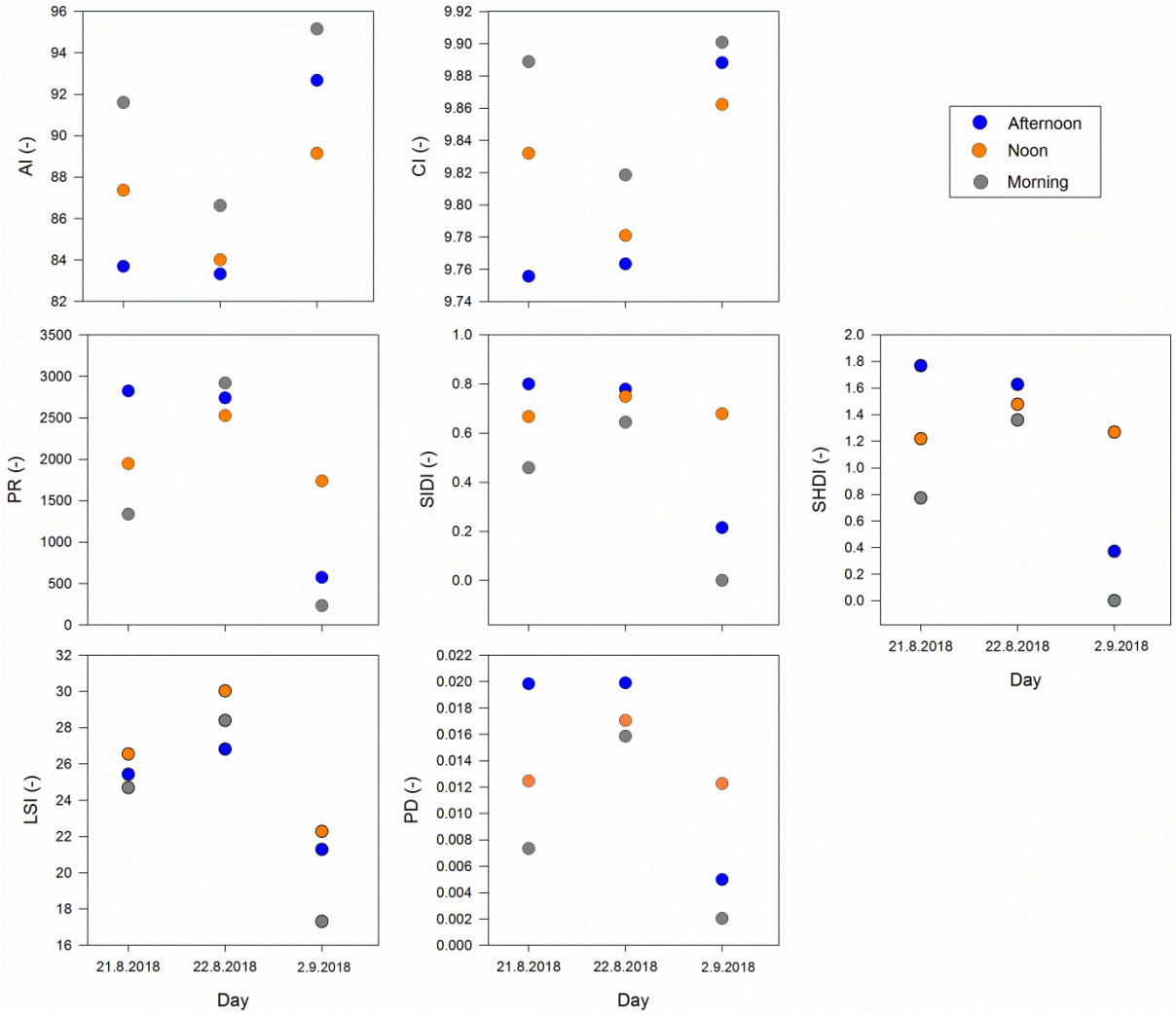

Figure 15. Landscape metrics for corrected radiant temperature (T_r) over the entire study reach in the morning, at noon and in the afternoon of August 21 (sunny), August 22 (sunny) and September 2 (cloudy). The seven metrics include the thermal aggregation index (AI), thermal cohesion index (CI), thermal patch richness (PR), Simpson's thermal diversity index (SIDI), Shannon's thermal diversity index (SHDI), thermal landscape shape index (LSI) and thermal patch density (PD). Please note the different y-axis scales. See Table 1 for exact flight times and Figures 12 & F1 (appendix F) for corresponding TIR orthoimages.

As part of this study, levelplots were also developed, which were a very useful representation for analysing thermal variation of radiant surface temperatures over the entire study reach (Fig. 16). In figure 16, it is possible to see the warming effect from morning to afternoon, the slight longitudinal cooling effect from upstream to downstream and the greater thermal heterogeneity of the two sunny days. Moreover, it can also be seen that the water temperature is slightly warmer on the right than on the left side of the river (sunny days, afternoon in Fig. 16).

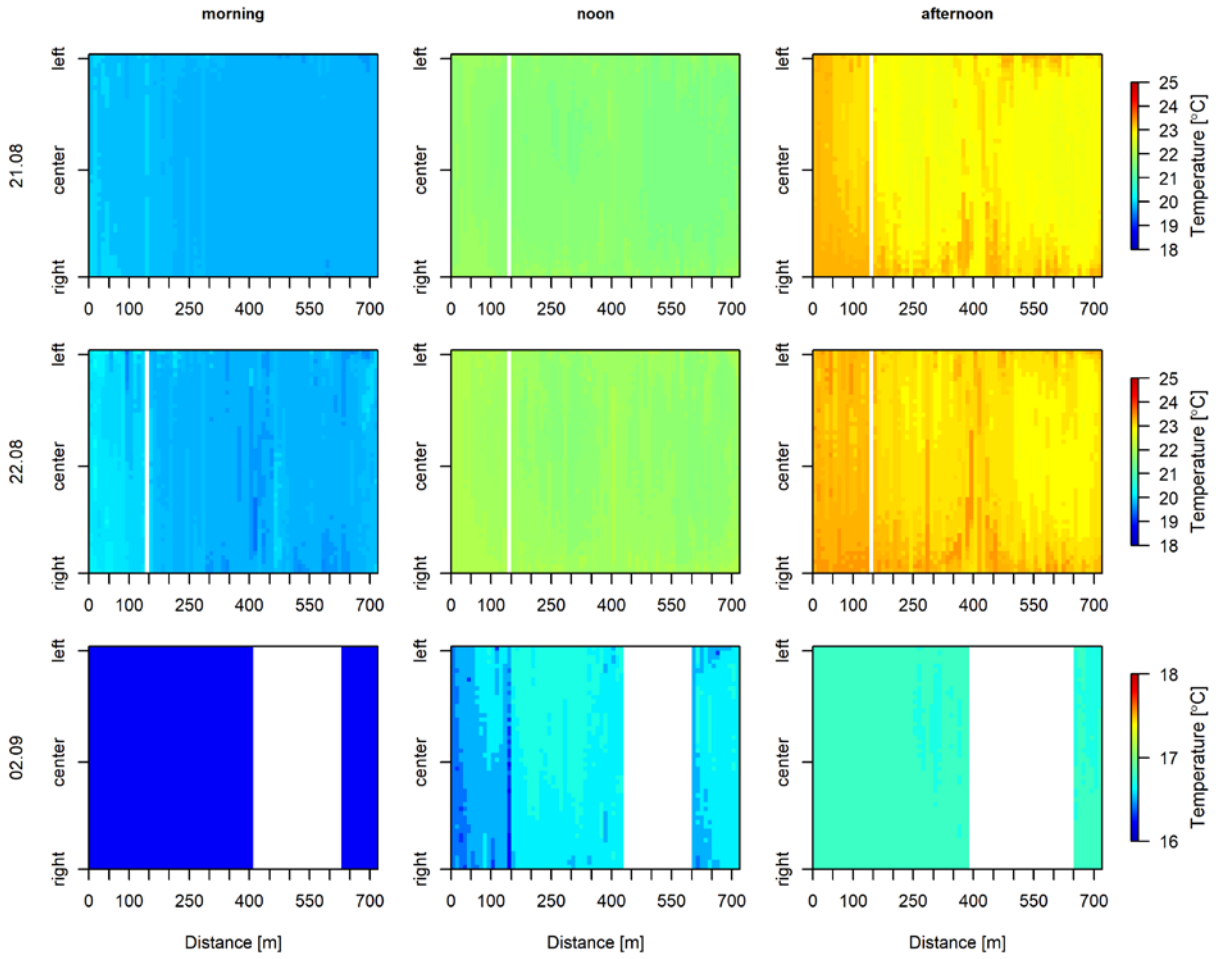

Figure 16. Levelplots of corrected thermal variation of radiant surface temperature (Tr) with pixels (n > 100'000) of the entire TIR orthoimage in the morning, at noon and in the afternoon of August 21 (sunny), August 22 (sunny) and September 2 (cloudy). White areas represent no data (feature matching not possible due to the ambient conditions on September 2 and bridge = no water pixels for August surveys). Flow direction is from left to right. Please note the different temperature scales on September 2. See Table 1 for exact flight times and Figures 12 & F1 (appendix F) for corresponding TIR orthoimages.

4.2.5 ADCP-Thermomaps

On the sunny day, the mean water T_k mapped using an ADCP mounted on a Hydroboard correlated very well with the measurements from the *in-situ* logger T_k (r^2 = 0.99; Fig. 17 left),

although ADCP-T_k was higher than the logger T_k (mean 0.46 ± 0.07 °C; range: 0.38 – 0.56 °C). This temperature difference was probably due to the spatial heterogeneity of the ADCP measurements (Fig. 17 right) and accuracy of both sensors (± 0.1 °C). Some spatial thermal heterogeneity was also confirmed by the drone TIR thermoscans (Appendix F, Fig. F5). Over the five sampling intervals on the cloudy day (11:15 – 13:15), both ADCP and the loggers delivered only slight temperature differences of approximately 0.1 °C, which correspond to the sensors' accuracies.

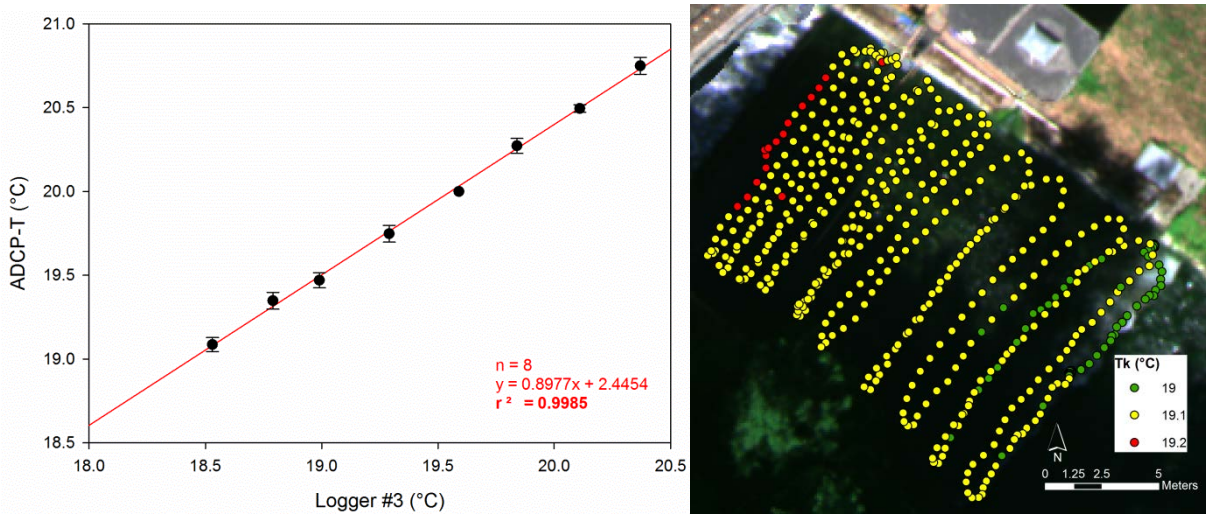

Figure 17. Left: Comparison between mean kinetic water temperature mapped with an ADCP and kinetic temperature measured by in-situ temperature logger #3 on August 12 (11:00-13:00; sunny). Error bars show the standard deviation of the ADCP measurements. Right: Example of the spatially continuous temperature data collected using the ADCP in one sec intervals (August 12 11:00). See Figure 2 for location of logger #3 and area mapped with the ADCP.

5 Discussion and Conclusions

Our study has proven multispectral and thermal infrared remote sensing to be a valuable tool for high temporal and spatial resolution quantitative assessment of riparian shading and instream temperatures. However, the study has also revealed some important considerations that should to be taken into account, which are outlined below.

5.1 Assessment of riparian shading using multispectral images

The application of **drone based high resolution multispectral data is well suited to the detection and quantification of riparian shading** in river systems. It was possible to quantify the shaded areas directly underneath the overhanging vegetation canopy using a

semi-automatic vegetation classification in combination with elevation information and some manual corrections. The extent of the oblique shadows cast by vegetation and topography could be quantified in the spectral data using segmentation, intensity mapping and some manual correction. The post-processing workflow presented in Figure 4 allowed **high spatial resolution shade distribution to be mapped and diurnal shade dynamics to be assessed** using multi-temporal drone flights. Furthermore, our study clearly showed **that shadows cast by vegetation and topography is extremely dynamic and can change considerably in just a few minutes** (Figs. 7 & 8). Therefore, we believe that **shade quantification performed with multispectral drone data is more precise and objective than field surveys**. It is particularly important to note that drone surveys can be performed on a large scale and at a high frequency, allowing this method to adjust to the quickly changing conditions mentioned above.

The selected study site on the Glatt River has been shown to pose certain challenges in terms of the optical permeability of the water due to its shallowness, the spectral heterogeneity (colour intensity and illumination properties) of the study reach and feature matching. Therefore, it was necessary to perform some manual steps and make manual corrections to the data in order to accurately quantify the shade. Landcover and shade classification was constrained by the complexity of the study area and the fact that the high resolution of the drone imagery made fully automatic classification challenging. However, in addition to the spectral information, drone surveys also provide spatial information e.g. points clouds and surface models. Combining this information has been shown to improve automatic landcover classification (e.g. Milani et al. 2018) and could also improve shade detection and quantification in more heterogeneous areas.

5.2 Assessment of water temperature using thermal infrared images

The use of a high-end **stationary thermal infrared (TIR) camera allowed very accurate measurements of surface water temperature** to be made (Fig. 11). Application of such cameras at fixed locations (e.g. gauging stations) in well-mixed rivers represents a promising solution for continuous measurement and monitoring of water temperature. However, before the general suitability and reliability of such measurements can be established, **tests over a**

longer period and under different meteorological and hydrological conditions (possibly also at different study sites and with different TIR cameras) **should be performed**.

The application of **drone based TIR data is well suited to the detection and quantification of longitudinal and lateral thermal patterns (2D) and the temporal dynamic of surface water temperature** in well-mixed river systems (Figs. 12-16). Our study applied and further developed several analysis tools for cold-water detection (Fricke & Baschek 2015; Wawrzyniak et al. 2016; levelplots; Chap. 3.2.2). However, cold water inflow or patches of cold water were not detected in the study reach. The discharge of the small cold-water side channels found in the study reach (Chap. 3.2.2) was probably not large enough to considerably change the water temperature of the Glatt River and no substantial effects of shade on the water temperature were detectable because the residence time of water was very short (straight channel with no large pools and mainly fast flowing water). Nevertheless, we believe that **remotely sensed TIR imagery is well suited to 2D detection of surface temperature differences (suggestion: ± 0.5 – 1 °C). Furthermore, it is a reliable method for acquiring information at a scale detailed enough for the detection of cold (e.g. groundwater or tributary) or warm (e.g. wastewater or other industrial waters) water inflows and ecologically relevant thermal refuges** (e.g. Torgersen et al. 2001; Tonolla et al. 2012; Deitchman & Loheide 2009; Wawrzyniak et al. 2013; Eschbach et al. 2016; Fullerton et al. 2018), which may be critical for the survival of many biota, including fish. However, TIR imagery is less suitable for taking absolute temperature measurements, and there are certain limitations and considerations that need to be considered when applying thermal infrared measurements in fluvial environments in order to ensure that the data acquired is of reasonable quality and that appropriate analysis can be carried out.

The selected study site of the Glatt River posed a number of challenges because of the low water level (exposed sediment), overhanging vegetation and the large number of algae and macrophytes, which ultimately complicated the definition of pure-water pixels and the corresponding correct temperature signature. Moreover, the acquisition of thermal images under different meteorological (sunny vs. cloudy) and day-time conditions (e.g. humidity, wind, sky radiation) influenced atmospheric absorption and emissions and ultimately the accuracy and comparability of the TIR measurements. Therefore, ***in-situ*** **temperature measurements (e.g. loggers) are absolutely necessary to validate and correct surface**

water radiant temperatures estimated by means of infrared thermography. In our study, realistic thermal infrared errors were estimated to be ± 0.5 °C (Chap. 4.2.1), which agrees with several other studies (Torgersen et al. 2001; Wawrzyniak et al. 2013; Lee et al. 2016). Moreover, *in-situ* temperature measurements provided critical information on the temporal thermal dynamic of the water.

An alternative for the characterization of 2D temperature patterns, especially in complex rivers (narrow valley, overhanging vegetation with sediment, algae and macrophytes exposed above the water's surface) where thermal remote sensing survey is not feasible or data analysis is extremely challenging, is the **use of an Acoustic Doppler Current Profiler** (ADCP) **temperature sensor** mounted to a board and synchronized with a differential GPS (sub-meter position accuracy; Chap. 4.2.5). Our study showed the potential of this method, possibly also in combination with a fast-tracking thermometer (temperature response time 0.1 sec), for spatio-temporal analysis of river temperatures (i.e. thermomaps).

General suggestions and further applications

For a comprehensive thermal characterization of complex river systems, and in order to assess thermal patterns that could affect the distribution of biota and ecosystem processes, both spatially and temporally, extensive temperature surveys may be required. For river surveys with remotely sensed TIR imagery, it is possible to make the following **general suggestions** (site and study goal specific):

- perform mid-afternoon TIR surveys when the water temperature can be expected to be more stable, near the daily maximum which is likely to be most limiting to aquatic biota. Alternatively, perform late afternoon-evening (after sunset) surveys when maximum thermal heterogeneity can be expected and in order to minimize erroneous temperature measurements caused by solar reflection;
- perform parallel multispectral and TIR surveys between 13:00 and 16:00 when the windows of optimum illumination and river temperature overlap.
- conduct TIR surveys when river discharge is low and stable in order to reveal thermal heterogeneity resulting from local variability of radiative warming and advective heat contributions (Dugdale et al. 2016);
- perform TIR surveys under the following conditions: short measurement distances (< 300 m), low humidity (< 50% relative humidity), low wind (< 15 m/s), low sensor angle (≤ 30°,

better nadir or near nadir, e.g. 7°) and low water turbidity (inorganic sediment, clay-silt concentrations < 50'000 mg/L) in order to reduce problems linked to atmospheric and background effects, emissivity and surface characteristics (Appendices in Tonolla et al 2010, 2012).

TIR imagery also has great potential for a broad range of **further applications**:

- quantification and dense monitoring of surface water temperature in medium to large rivers and lakes. Advantages: sufficient pure-water pixels and fewer environmental effects than in small streams;
- calibration, validation and improvement of stream temperature models (e.g. Cristea & Burges 2009; Loheide & Gorelick 2006; Cardenas et al. 2014). We are currently collaborating with EAWAG to evaluate the thermal effect (i.e. thermopeaking) of water inflow near hydropower plants using a combination of remotely sensed TIR imagery, 2D thermal modelling and in-situ surveys;
- monitoring the success of restoration projects, for example in terms of cold-water thermal refuges for fishes.

In conclusion, we consider the two recent studies by Wawrzyniak et al. (2016; characterization of temporal variability and spatial distribution of cold water patches along a 50 km river reach) and Fullerton et al. (2018; characterization of frequency, size, and spacing of cool thermal patches suitable for Pacific salmon along 11'308 km of 2nd–7th order rivers and the potential influences of climate change on availability of cool patches) to be excellent examples of the effective use of remotely sensed TIR imagery in river management and fundamental fluvial science that can also be applied in Switzerland. Finally, the fast pace of drone and sensor technology development has the potential to enable more frequent, automatic and precise thermal assessments and efficient mapping of larger freshwater areas to be carried out.

6 Literatur

Adeline KRM, Chen M, Briottet SK, Pang N. Paparoditis 2013. Shadow detection in very high spatial resolution aerial images: a comparative study. *ISPRS Journal of Photogrammatry and Remote Sensing* 80: 21–38.

Andrews BJ, Cardenas MB, Bennett PC. 2011. Analysis of turbulent non-isothermal mixing between a jet and cooler ambient water using thermal imagery. *Geochemistry, Geophysics, Geosystems* 12: Q07022.

Arscott DB, Tockner K, & Ward JV. 2001. Thermal heterogeneity along a braided floodplain river (Tagliamento River, northeastern Italy). *Canadian Journal of Fisheries and Aquatic Sciences* 58: 2359–2373.

Buisson L, Blanc L, Grenouillet G. 2008. Modelling stream fish species distribution in a river network: the relative effects of temperature versus physical factors. *Ecology of Freshwater Fish* 17: 244–257.

Caissie D. 2006. The thermal regime of rivers: A review. *Freshwater Biology* 51: 1389–1406.

Cardenas MB, Doering M, Rivas DS, Galdeano C, Neilson BT, Robinson CT. 2014. Analysis of the temperature dynamics of a proglacial river using time-lapse thermal imaging and energy balance modeling. *Journal of Hydrology* 519: 1963–1973.

Cardenas MB, Neale CMU, Jaworowski C, Heasler H. 2011. High-resolution mapping of river-hydrothermal water mixing: Yellowstone National Park. *International Journal of Remote Sensing* 32: 2765–2777.

Cristea NC, Burges SJ. 2009. Use of thermal infrared imagery to complement monitoring and modeling of spatial stream temperatures. *Journal of Hydrologic Engineering* 14: 1080–1090.

Deitchman RS, Loheide SP. 2009. Ground-based thermal imaging of groundwater flow processes at the seepage face. *Geophysical Research Letters* 36: L14401.

Dugdale SJ. 2016. A practitioner's guide to thermal infrared remote sensing of rivers and streams: recent advances, precautions and considerations. *WIREs Water*. Doi: 10.1002/wat2.1135.

Eschbach D, Piasny G, Schmitt L, Pfister L, Grussenmeyer P, Koehl M, Skupinski G, Serradj A. 2017. Thermal-infrared remote sensing of surface water-groundwater exchanges in a restored anastomosing channel (Upper Rhine River, France). *Hydrological Processes* 31: 1113–1124.

Faux RN, Maus P, Lachowsky, H, Torgersen CE, Boyd MS. 2001. New approaches for monitoring stream temperature: airborne thermal infrared remote sensing. *Inventory and monitoring project report*, integration of remote sensing, Remote sensing applications center, USDA Forest service engineering.

Faye E, Rebaudo F, Yánez-Cajo D, Cauvy-Fraunié S, Dangles O. 2016. A toolbox for studying thermal heterogeneity across spatial scales: from unmanned aerial vehicle imagery to landscape metrics. *Methods in Ecology and Evolution* 7: 437–446.

FOEN 2018a. Hydrological data service for watercourses and lakes. Dicharge data of the gauging station Glatt – Rheinsfelden (nr. 2415). *Federal Office for the Environment*. https://www.hydrodaten.admin.ch/en/2415.html.

FOEN 2018b. Hydrological data service for watercourses and lakes. Water quality statistics (state July 1 2016) of the gauging station Glatt – Rheinsfelden (nr. 2415). *Federal Office for the Environment*. https://www.hydrodaten.admin.ch/en/2415.html.

FOEN 2018c. Modelled mean runoff and flow regime types for the river network of Switzerland. *Federal Office for the Environment*. https://map.geo.admin.ch/.

Fricke K, Baschek B. 2015. Temperature monitoring along the Rhine River based on airborne thermal infrared remote sensing: estimation of in-situ water temperatures and inflow detection compared to artificial satellite data. *Journal of Applied Remote Sensing* 9: 095067.

Fullerton AH, Torgersen CE, Lawler JJ, Steel EA, Ebersole, JL, Lee SY. 2018. Longitudinal thermal heterogeneity in rivers and refugia for coldwater species: effects of scale and climate change. *Aquatic Sciences* 80: 3.

Ginzler C, Hobi ML. 2015. Countrywide stereo-image matching for updating digital surface models in the framework of the Swiss National Forest Inventory. *Remote Sensing*, 7: 4343–4370.

Hijmans RJ. 2017. Raster: geographic data analysis and modeling. https://cran.r-project.org/package=raster.

IPCC. 2014. Fifth assessment report on climate change. *The Intergovernmental Panel of Climate Change*. http://www.ipcc.ch/.

Johnson SL. 2004. Factors influencing stream temperatures in small streams: substrate effects and a shading experiment. *Canadian Journal of Fisheries and Aquatic Sciences* 61: 913–923.

Killick R, Eckley I. 2014. Changepoint: an R package for changepoint analysis. *Journal of Statistical Software*: 58: 1–19.

Lebourgeois V, Labbé S, Jacob F, Bégué A. 2008. Atmospheric corrections of low altitude thermal infrared airborne images acquired over a tropical cropped area. *International Geoscience Remote Sensing Symposium*, Boston, USA.

Lee E. Yoon H, Hyun SP, Burnett WC, Koh DC, Ha K, Kim DJ, Kim Y, Kang KM. 2016. Unmanned aerial vehicles (UAVs)-based thermal infrared (TIR) mapping, a novel approach to assess groundwater discharge into the coastal zone. *Limnology and Oceanography Methods*: 14: 725–735.

Lillesand TM, Kiefer RW, Chipman JW. 2008. Multispectral, thermal, and hyperspectral sensing. In Lillesand TM, Kiefer RW, Chipman JW (Eds.). *Remote Sensing and Image Interpretation*, New York: JohnWiley & Sons.

Loheide SP, Gorelick SM. 2006. Quantifying stream-aquifer interactions through analysis of remotely sensed thermographic profiles and in-situ temperature histories. *Environmental Science and Technology* 40: 3336–3341.

Ma H, Qin Q, Shen X. 2008. Shadow segmentation and compensation in high resolution satellite images. *Geoscience and Remote Sensing Symposium*, IGARSS 2008. IEEE International, Vol. 2, pp. II-1036.

Madej MA, Currens C, Ozaki V, Yee J, Anderson DG. 2006. Assessing possible thermal rearing restrictions for juvenile coho salmon (*Oncorhynchus kisutch*) through thermal infrared imaging and in-stream monitoring, Redwood Creek, California. *Canadian Journal of Fisheries and Aquatic Sciences* 63: 1384–1396.

Magnuson JJ, Crowder LB, Medvick PA. 1979. Temperature as an ecological resource. *American Zoologist* 19: 331–343.

Malard F, Mangin A, Uehlinger U, Ward JV. 2001. Thermal heterogeneity in the hyporheic zone of a glacial floodplain. *Canadian Journal of Fisheries and Aquatic Sciences* 58: 1319–1335.

McCullough DA, Bartholow JM, Jager HI, Beschta RL, Cheslak EF, Deas ML, et al. 2009. Research in thermal biology: burning questions for coldwater stream fishes. *Reviews in Fisheries Science* 17: 90–115.

Milani G, Volpi M, Tonolla D, Doering M, Robinson C, Kneubühler M, Schaepman M. 2018. Robust quantification of riverine land cover dynamics by high-resolution remote sensing. *Remote Sensing of Environment* 217: 491–505.

Movia A, Beinat A, Crosilla F. 2016. Shadow detection and removal in RGB VHR images for land use unsupervised classification. *ISPRS Journal of Photogrammatry and Remote Sensing* 119: 485–495.

PIX4D. 2018. Pix4D Mapper Software v.4.3.31. https://www.pix4d.com/product/pix4dmapper-photogrammetry-software.

Polidorio AM, Flores FC, Imai NN, Tommaselli AM, Franco C. 2003. Automatic shadow segmentation in aerial color images. Computer Graphics and Image Processing. *Proceeding of the XVI Brazilian Symposium on Computer Graphics and Image processing*: 270-277.

R Core Team. 2018. A Language and Environment for Statistical Computing. https://www.r-project.org.

Rikimaru A, Roy PS, Miyatake S. 2002. Tropical forest cover density mapping. *Tropical Ecology* 43: 39–47.

Rutherford JC, Blackett S, Blackett C, Saito L, Davies-Colley RJ. 1997. Predicting the effects of shade on water temperature in small streams. *New Zealand Journal of Marine and Freshwater Research* 31: 707–721.

Rutherford JC, Marsh N, Davies P, Bunn S. 2004. Effects of patchy shade on stream water temperature: how quickly do small streams heat and cool? *Marine and Freshwater Research* 55: 737–748.

Shuman CS, Ambrose RF. 2003. A comparison of remote sensing and ground-based methods for monitoring restoration success. *Restoration Ecology* 11: 325–333.

Tonolla D, Acuña V, Uehlinger U, Frank T, Tockner K. 2010. Thermal heterogeneity in river floodplains. *Ecosystems* 13: 727–740.

Tonolla D, Wolter C, Ruhtz T, Tockner K. 2012. Linking fish assemblages and spatio-temporal thermal heterogeneity in a river-floodplain landscape using high-resolution airborne thermal infrared remote sensing and in-situ measurements. *Remote Sensing of Environment* 125: 134–146.

Torgersen CE, Baxter CV, Li HW, McIntosh BA. 2006. Landscape influences on longitudinal patterns of river fishes: spatially continuous analysis of fish-habitat relationships. *In* Hughes RM, Wang L,

Seelbach PW (Eds.), Landscape Influences on Stream Habitats and Biological Assemblages. *American Fisheries Society, Symposium* 48, Bethesda, Maryland, USA.
Torgersen CE, Faux RN, McIntosh BA, Poage NJ, Norton DJ. 2001. Airborne thermal remote sensing for water temperature assessment in rivers and streams. *Remote Sensing of Environment* 76: 386–398.
Torgersen CE, Price DM, Li HW, McIntosh BA. 1999. Multiscale thermal refugia and stream unit associations of chinook salmon in northeastern Oregon. *Ecological Applications* 9: 301–319.
VanDerWal J, Falconi L, Januchowski S, Shoo L, Storlie C. 2014. SDMTools: Species Distribution Modelling Tools: tools for processing data associated with species distribution modelling exercises. https://cran.r-project.org/package=SDMTools.
Wawrzyniak V, Piégay H, Allemand P, Vaudor L, Goma R, Grandjean P. 2016. Effects of geomorphology and groundwater level on the spatio-temporal variability of riverine cold water patches assessed using thermal infrared (TIR) remote sensing. *Remote Sensing of Environment* 175: 337–348.
Wawrzyniak V, Piégay H, Allemand P, Vaudor L, Grandjean P. 2013. Prediction of water temperature heterogeneity of braided rivers using very high resolution thermal infrared (TIR) images. *International Journal of Remote Sensing* 34: 4812–4831.
Webb BW. 1996. Trends in stream and river temperature. *Hydrological Processes* 10: 205–226.
Webb BW, Clack PD, Walling DE. 2003. Water-air temperature relationships in a Devon river system and the role of flow. *Hydrological Processes* 17: 3069–3084.
Webb BW, Zhang Y. 1999. Water temperatures and heat budgets in Dorset chalk water courses. *Hydrological Processes* 13 309–321.
Wolter C. 2007. Temperature influence on the fish assemblage structure in a large lowland river, the lower Oder River, Germany. *Ecology of Freshwater Fish* 16: 493–503.

7 Appendix

7.1 Appendix A: Technical specifications of the cameras used

Multispectral camera

The multispectral MicaSense RedEdge™ camera has a lens focal length of 5.5 mm, a field of view of 87.4°and includes five spectral bands: blue (Band 1: 460–510 nm), green (Band 2: 545–575 nm), red (Band 3: 630–690 nm), NIR (Band 4: 820–860 nm) and red-edge (Band 5: 712–722 nm).

Drone thermal infrared camera

The thermamap™drone thermal infrared camera has an uncooled 14-bit Vanadium Oxide microbolometer focal-plan-array detector operating in the 7.5–13.5 µm spectral range. The camera has a field of view of 69° x 56° with a horizontal resolution of 1.889 mrad and an image size of 640 pixels x 512 scanning lines. Emissivity of the camera is automatically set to 1 (i.e. perfect absorber/radiator) and cannot be modified. To calibrate absolute temperature accuracy, a shutter is regularly closed in-flight (at a known temperature). Optical calibration (camera internal orientation, focal plane, etc.) is performed during the post-processing

workflow. The camera has a fixed focus allowing a flight operation altitude between 40 and 150 m.

Stationary thermal camera

The stationary thermal camera has an internally calibrated focal plane array, uncooled microbolometer operating in the 7.5–14 µm spectral range. The camera has a field of view of 45° x 34° with a horizontal resolution of 1.3 mrad and an image size of 640 pixels x 480 scanning lines. Atmospheric transmission correction for this camera is automatic and based on inputs for distance, atmospheric temperature and relative humidity. To be consistent with thermal images acquired by the drone an emissivity value of 1 was set.

7.2 Appendix B: Water mask

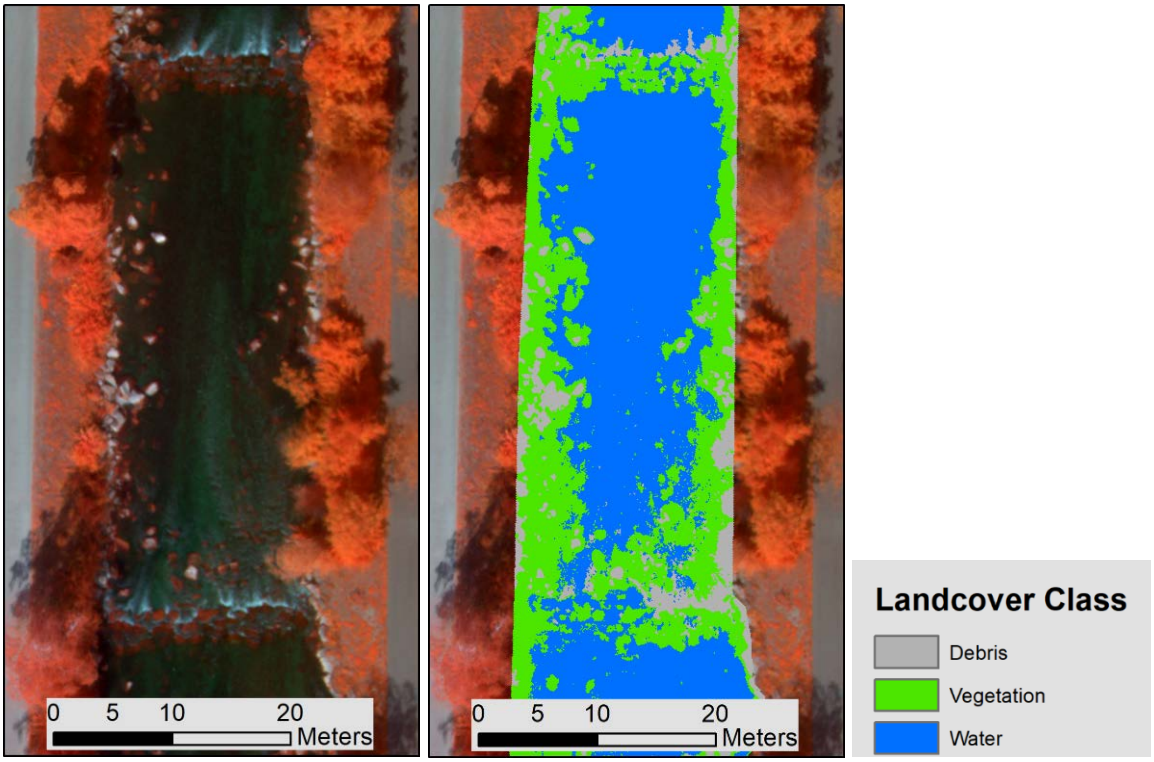

Figure B1. Pronounced example of how the masking of the water area underestimated the actual water surface. Therefore, an aggressive filtering/masking was necessary to ensure reliable analysis of the actual water area.

7.3 Appendix C: Loggers accuracy, thermal stratification and side channels

Logger accuracy

Table C1. Logger inter-accuracy was checked in a temperature-controlled water bath using the average temperature of all the loggers minus the average temperature of each single logger. L#: logger number. See Figure 2 (main text) for logger locations. Logger #12 was either lost as the result of a small flood event on August 14 2018 (ca. 20.5 m^3/s) or because of human intervention.

L #	Inter-accuracy (°C)
1	-0.09
2	-0.02
3	0.05
4	-0.07
5	-0.01
6	-0.07
7	-0.07
8	0.08
9	0.17
10	-0.05
11	0.05
13	0.02
14	-0.08
15	-0.08
16	0.04
17	0.03
18	0.08
19	0.01

Thermal stratification

Measurements of thermal stratification were conducted on the survey dates of August 12, August 21 and September 2. Water T_k was measured at each temperature logger location at approximately 10 cm below the water surface and at 10 cm above the river bottom with a Flowatch Flowmeter (JDC Electronic SA; resolution 0.1 °C, accuracy ± 0.2 °C, manufacturer's specifications). Thermal stratification was then calculated as the surface T_k minus the bottom T_k = T_s (Tab. C2). The water was considered stratified when T_s exceeded the ± 0.2 °C accuracy of the sensor.

Table C2. Thermal stratification at individual logger locations on three survey dates. T_s = surface T_k – bottom T_k, representing the stratification temperature threshold (i.e., stratified when T_s > 0.2 °C). L#: logger number; NA: not available; h: water depth; v: flow velocity measured at ca. 60% water depth with a SonTek FlowTracker 2 (Xylem Inc., San Diego, CA, USA; resolution 0.0001 m/s, accuracy ±1% of measured velocity, manufacturer's specifications). See Figure 2 (main text) for logger locations.

L #	Habitat type	Thermal stratification T_s (°C)			h (m)	v (m/s
		12.08.2018 (14:35-15:40)	21.08.2018 (12:50-16:40)	02.09.2018 (10:20-15:15)	21.08.2018	
1	Run	0.0	0.0	0.0	0.46	0.24
2	Fast flowing run	0.0	0.0	0.0	0.62	0.54
3	Run	0.1	0.0	0.0	0.60	0.20
4	Backwater	0.0	0.2	0.0	0.26	0.30
5	Riffle/step	-0.1	0.0	0.1	0.68	0.06
6	Riffle/step	0.1	0.0	0.0	0.56	0.44
7	Fast flowing run	-0.1	0.0	-0.1	0.40	0.42
8	Fast flowing run	0.2	0.0	0.0	0.76	0.35
9	Run	-0.1	0.0	0.1	0.44	0.01
10	Standing pool	0.0	0.0	0.0	0.14	0.04
11	Slow flowing pool	0.0	0.0	0.0	0.24	0.05
12	Fast flowing run	-0.1	NA	NA	NA	NA
13	Slow flowing pool	-0.1	0.0	0.0	0.48	0.06
14	Run	0.0	0.0	0.0	0.30	0.23
15	Fast flowing run	0.1	0.0	0.1	0.52	0.57
16	Pool	-0.1	0.1	0.0	0.78	0.23
17	Fast flowing run	0.0	0.0	-0.1	0.46	0.32
18	Run	0.0	0.0	0.0	0.14	0.03
19	Fast flowing run	0.0	0.0	0.0	1.10	0.30

Logger locations and side channels

The logger locations were determined for each survey date with a RTK-GPS (Trimble R10, Trimble Inc., Sunnivale, CA, USA; horizontal accuracy during the surveys < ±3 cm). Additionally, the locations of side channels that could influence the water temperature of the main channel were measured on August 22.

16 side channels, 13 on the left side of the river and three on the right side of the river, were found during the field survey (Fig. 2 main text) and their temperature was measured with a Flowatch Flowmeter (JDC Electronic SA; resolution 0.1 °C, accuracy ± 0.2 °C, manufacturer's specifications) (Tab. C3).

Table C3. Temperature of side channels on August 22, 2018 (10:40 – 13:40). L: side channel on the left side of the river; R: side channel on the right side of the river. L12 is where Logger #18 was located. NA: not available. Water temperature measured with a Flowatch Flowmeter (JDC Electronic SA; resolution 0.1 °C, accuracy ± 0.2 °C, manufacturer's specifications). See Figure 2 (main text) for side channel locations.

Side channel	Temperature (°C)	Comments
L1	13.9	
L2	12.6	
L3	14.8	
L4	14.6	
L5	14.5	
L6	14.3	
L7	14.5	
L8	15.0	
L9	14.2	
L10	14.9	
L11	16.0	
L12	16.1	
L13	NA	Street pipe, dry on August 22 2018
R1	15.5	
R2	NA	Street pipe, dry on August 22 2018
R3	NA	Street pipe, dry on August 22 2018

7.4 Appendix D: Shade on August 21

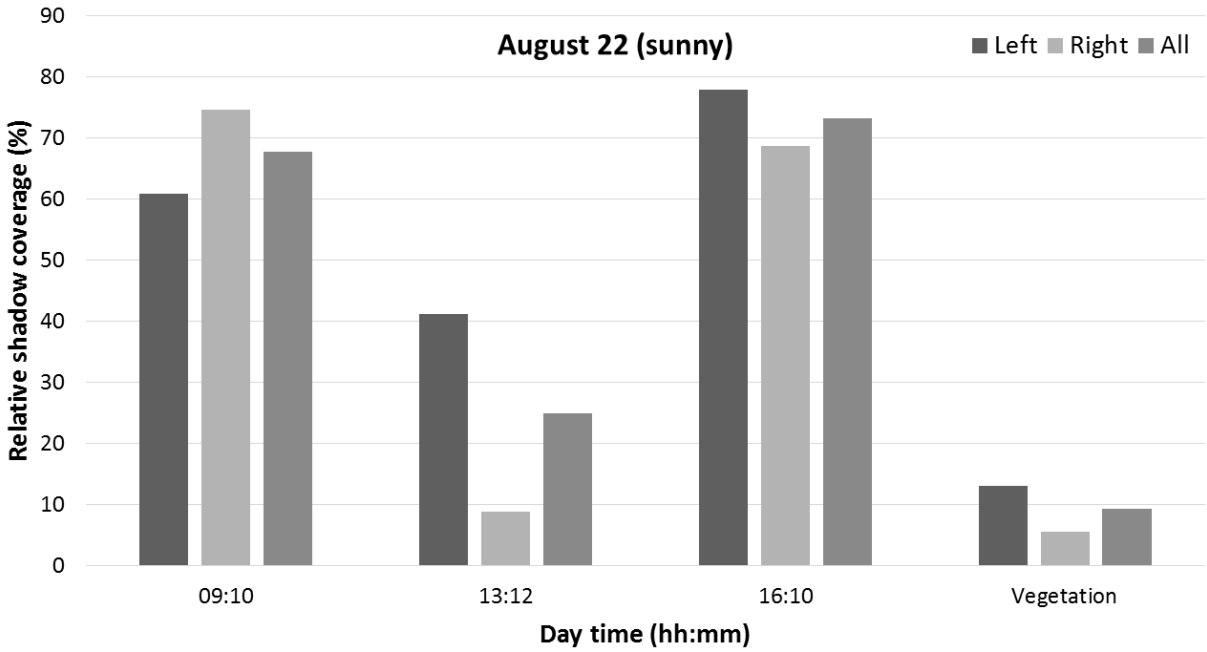

Figure D1. Percentage coverage of oblique shadows cast by vegetation and topography on the left and right sides of the rivers and the entire study area ("all"), and percentage coverage of the shaded area underneath the overhanging vegetation ("vegetation") on August 22 2018. Percentages relative to area covered.

7.5 Appendix E: Temporal dynamic of water temperature

*Table E1. Characterization of the temporal dynamic of water temperature (°C) by each in-situ logger. Recording period lasted from August 7, 2018 at 23:47 until September 2, 2018 at 16:13. L#: logger number; T_{kMin}: minimum kinetic temperature; T_{kMax}: maximum kinetic temperature; T_{kAv}: average kinetic temperature; T_{kAmp}: kinetic temperature amplitude; T_{kHeat}: maximum kinetic rate of thermal heating; T_{kCol}: maximum kinetic rate of thermal cooling; T_{kCum}: cumulative kinetic degree-days; T_{kCum24}: cumulative kinetic degree-days above 24 °C; T_{kCum20}: cumulative kinetic degree-days below 20 °C. Logger #12 was either lost as the result of a small flood event on August 14, 2018 (ca. 20.5 m3/s) or due to human intervention. Log*ger #2 was replaced on August 17, 2018, resulting in the loss of 37% of the data. *See Figure 2 (main text) for logger locations.*

L #	T_{kMin}	T_{kMax}	T_{kAv}	T_{kAmp}	T_{kHeat}	T_{kCol}	T_{kCum}	T_{kCum24}	T_{kCum20}
1	16.1	23.5	20.1	7.5	0.8	-0.8	504.8	0	11
2	16.1	23.2	19.8	7.2	0.8	-0.8	320.2	0	8
3	16.1	23.9	20.2	7.8	0.9	-0.8	507.5	0	9
4	16.1	23.6	20.1	7.5	0.8	-0.8	505.8	0	11
5	16.1	23.6	20.1	7.6	0.9	-0.8	506.0	0	11
6	16.3	23.8	20.2	7.6	1.0	-0.6	507.6	0	9
7	16.1	23.9	20.2	7.8	0.9	-0.8	507.2	0	9
8	16.1	23.9	20.2	7.8	0.9	-0.8	507.3	0	9
9	16.1	23.6	20.2	7.6	0.9	-0.8	506.8	0	9
10	16.1	23.5	20.1	7.4	1.4	-0.8	505.8	0	11
11	16.1	24.2	20.3	8.1	1.0	-0.8	509.8	0	9
13	16.1	23.4	20.1	7.3	0.8	-0.8	504.3	0	11
14	16.1	24.2	20.4	8.1	0.9	-0.8	512.1	0	5
15	16.1	23.9	20.2	7.9	0.9	-0.8	508.7	0	9
16	16.0	23.2	19.9	7.1	0.8	-0.8	500.0	0	11
17	16.1	23.9	20.2	7.8	0.9	-0.7	507.7	0	9
18	15.4	21.5	16.1	6.0	3.2	-1.7	402.2	0	25
19	16.0	24.0	20.3	8.0	0.9	-0.7	509.4	0	7

7.6 Appendix F: Thermal infrared images collected using a drone

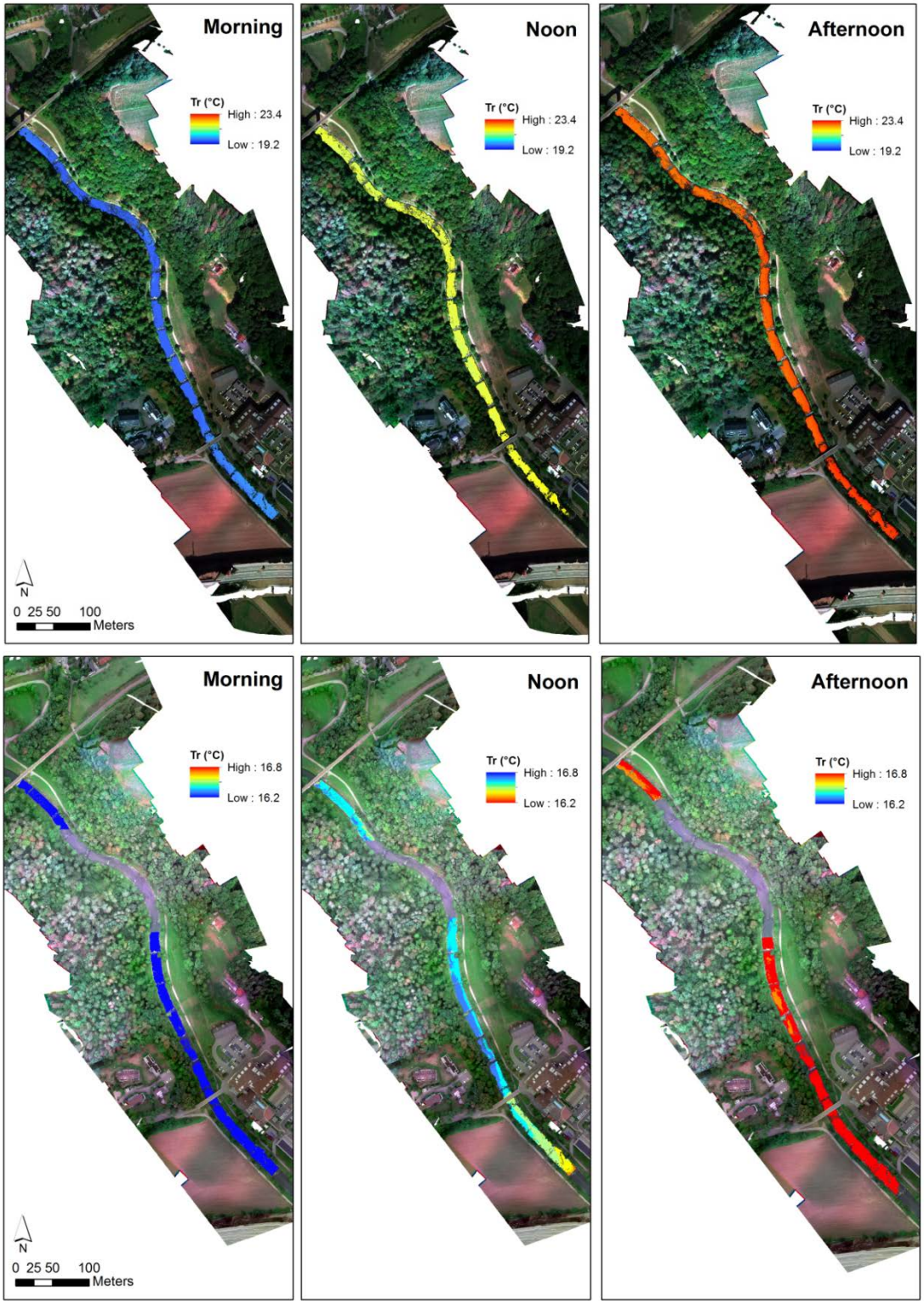

Figure F1. Temperature corrected TIR orthoimages (spatial distribution of radiant temperature (T_r) values per pixel) of the entire study reach in the morning, noon and afternoon of August 22, 2018 (top) and September 2, 2018 (bottom). Note that on the three images for each day, the temperature scale was kept constant for all three times of the day, See Table 1 (main text) for exact flight times. Flow direction is from south to north. Missing parts in the orthoimages from September 2 were due to impossible feature matching caused by the ambient conditions. Background maps: RGB orthoimages from August 21 and September 2, respectively.

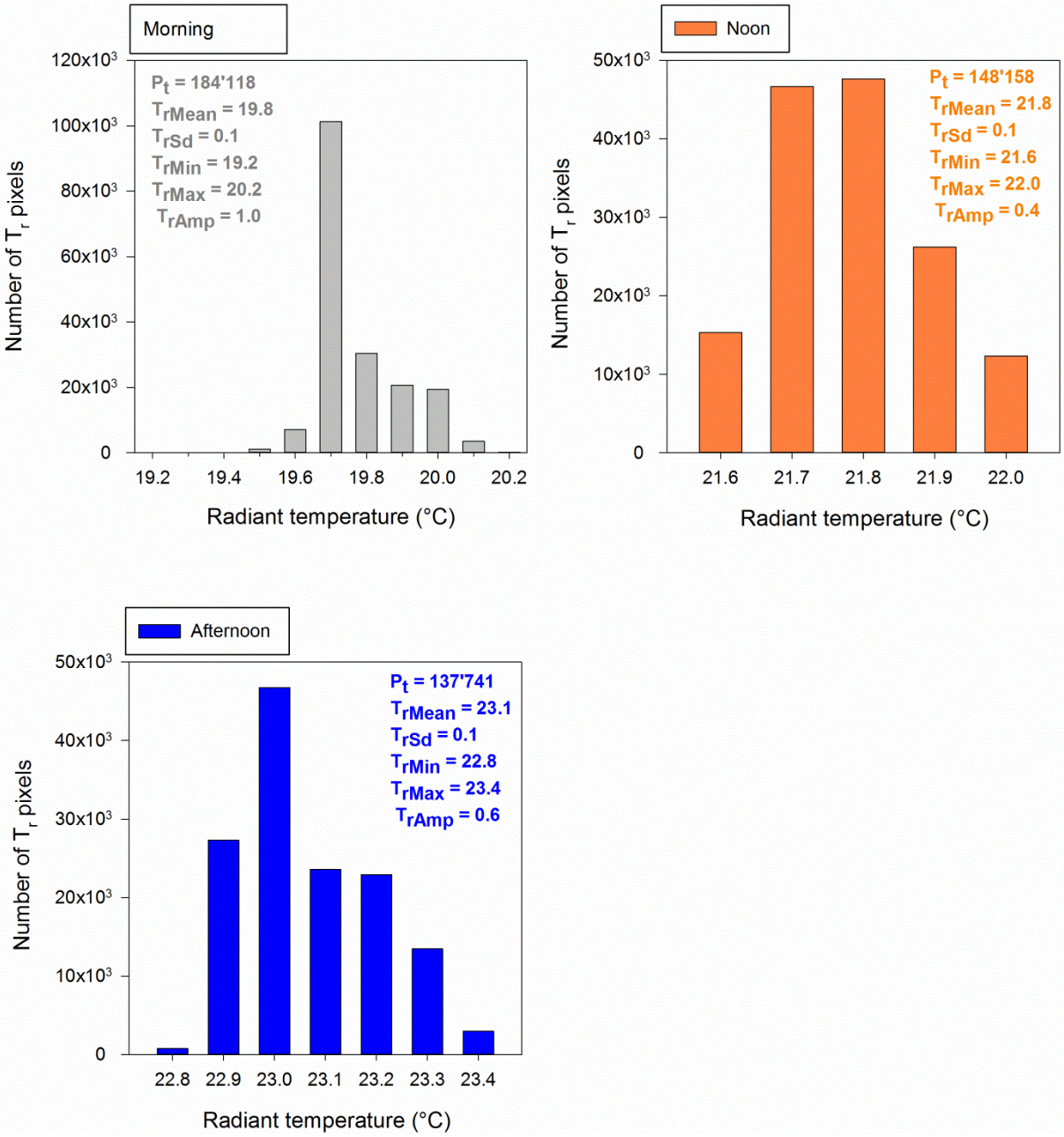

Figure F2. Pixel frequency distribution of corrected radiant temperature (T_r) over the entire study reach in the morning, at noon and in the afternoon of August 22, 2018 (sunny). Statistics for each histogram include six basic statistics: total number of pixels (P_t), mean radiant temperature (T_{rMean}), standard deviation of radiant temperature, (T_{rSd}), minimum radiant temperature (T_{rMin}), maximum radiant temperature (T_{rMax}) and radiant temperature amplitude (T_{rAmp}). Please note the different x- and y-axis scales. See Table 1 (main text) and Figure F1 for corresponding TIR orthoimages.

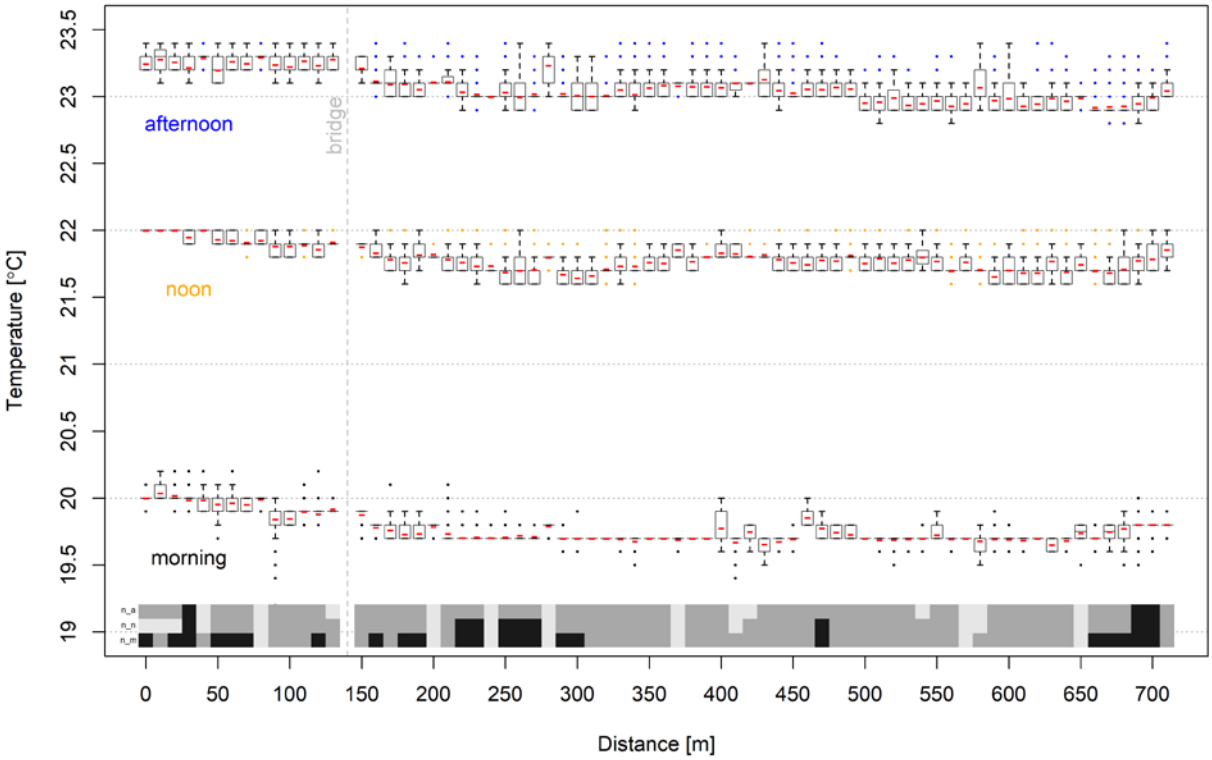

Figure F3. Corrected thermal gradients of the radiant surface temperature (T_r) of the entire study reach in the morning, at noon and in the afternoon of August 22, 2018. Boxplots represent temperature variations in 72 cross sections (spaced by 10 m) perpendicular to the ca. 750 m long reach. Boxplots show the 25th and 75th percentiles, median (black line in the box), mean (red line in the box), whiskers (25th - 1.5 x IQR; 75th + IQR) and outliers (dots). Grey-black boxes on the x-axis show the total number of pixels (n) in each boxplot (the darker the colour, the higher the "n" value) with n_a: afternoon, n_n: noon, n_m: morning. Flow direction is from left to right. See Table 1 (main text) for exact flight times and Figure F1 for corresponding TIR orthoimages.

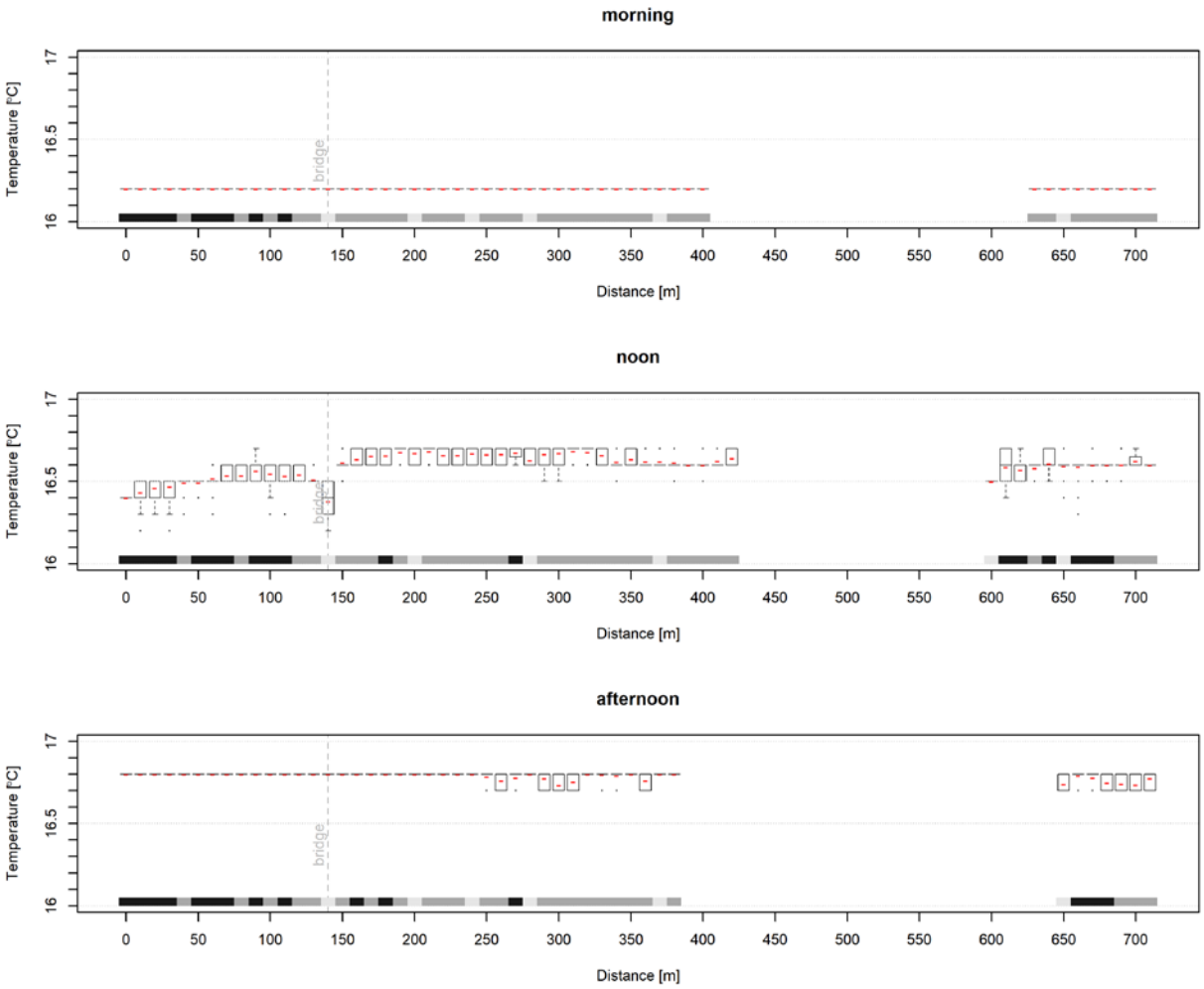

Figure F4. Corrected thermal gradients of the radiant surface temperature (T_r) of the entire study reach in the morning, at noon and in the afternoon of September 2, 2018. Boxplots represent temperature variations in 72 cross sections (spaced by 10 m) perpendicular to the ca. 750 m long reach. Boxplots show the 25th and 75th percentiles, median (black line in the box), mean (red line in the box), whiskers (25th - 1.5 x IQR; 75th + IQR) and outliers (dots). Grey-black boxes on the x-axis show the total number of pixels (n) in each boxplot (the darker the colour, the higher the "n" value) with n_a: afternoon, n_n: noon, n_m: morning. Flow direction is from left to right. See Table 1 (main text) and Figure F1 for corresponding TIR orthoimages. Missing sections between reach meter 400 and 650 were due to the inability to perform feature matching as a result of ambient conditions.

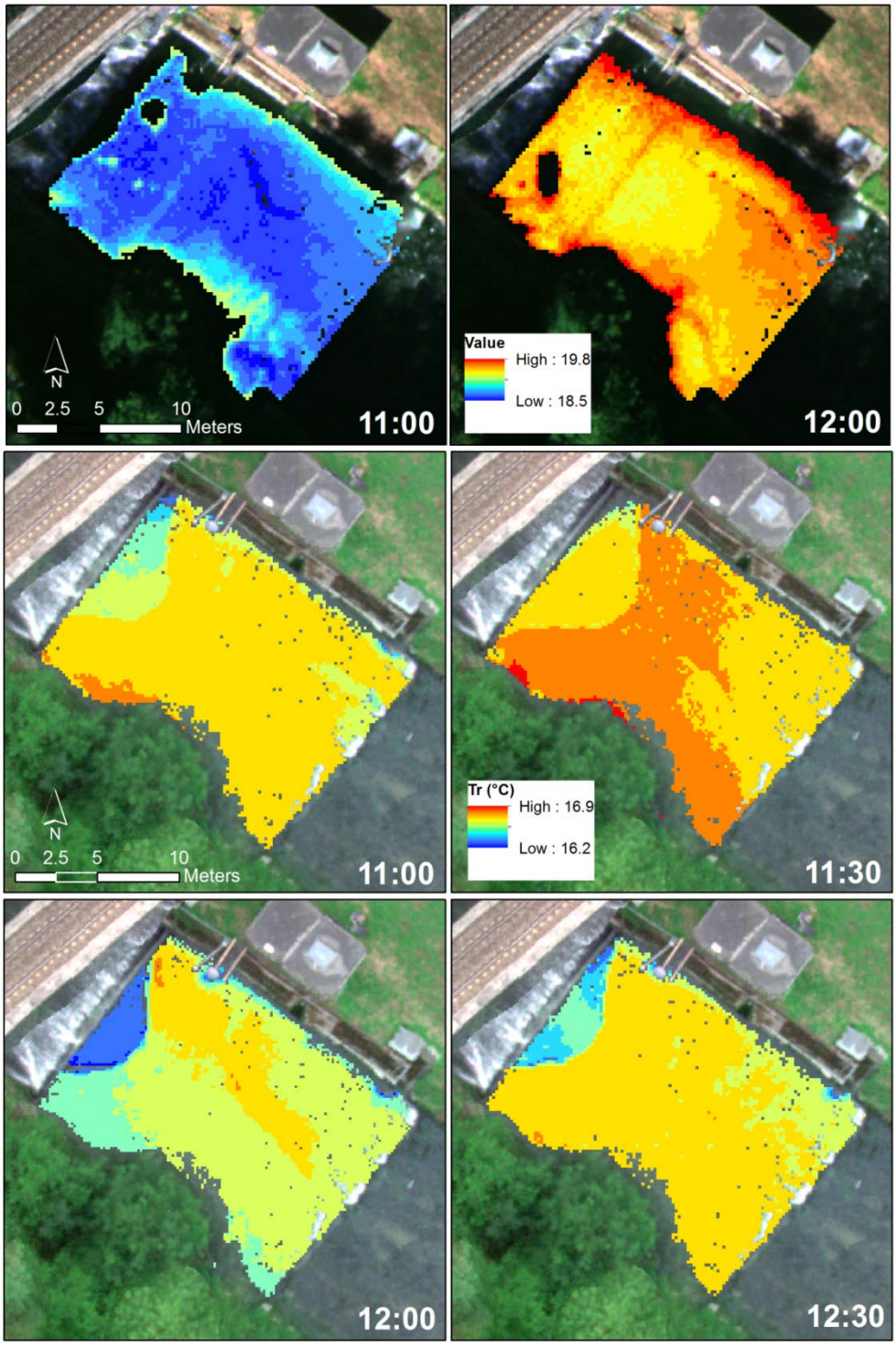

Figure F5. Drone TIR thermoscans. Temperature corrected TIR orthoimages (spatial distribution of radiant temperature, T_r, values per pixel) of the area between two artificial weirs in front of the gauging station. Top two images: August 12, 2018 (sunny; 11:00 – 12:00); Bottom four images: September 2, 2018 (cloudy; 11:00 – 12:30). Note that the temperature scale was kept constant for all times of each day. Flow direction is from right to left. Background maps: RGB orthoimages from August 12 and September 2, respectively. Note that most temperature differences in the images from September 2 are within the possible TIR image-error of ± 0.5 °C. Therefore, they probably do not represent real temperature differences. Moreover, reflection artefacts due to the railway bridge are also visible in these images.